Fall 11-15-2018

# Post-impact light vapor incorporation during lunar formation based on triple oxygen isotopes

Erick J. Cano
*University of New Mexico - Main Campus*

Erick Jason Akio Cano
*Candidate*

Earth and Planetary Sciences
*Department*

This thesis is approved, and it is acceptable in quality and form for publication:

*Approved by the Thesis Committee:*

Dr. Zachary Sharp, Co-Chairperson

Dr. Charles Shearer, Co-Chairperson

Dr. Jin Zhang

# POST-IMPACT LIGHT VAPOR INCORPORATION DURING LUNAR FORMATION BASED ON TRIPLE OXYGEN ISOTOPES

**by**

**ERICK JASON AKIO CANO**

**B.S, GEOLOGY, CALIFORNIA STATE UNIVERSITY, LONG BEACH, 2015**

THESIS

Submitted in Partial Fulfillment of the
Requirements for the Degree of

**Master of Science**
**Earth and Planetary Sciences**

The University of New Mexico
Albuquerque, New Mexico

**December, 2018**

# ACKNOWLEDGEMENTS:

First, I would like to thank all of my committee members, Dr. Zachary Sharp, Dr. Charles Shearer, and Dr. Jin Zhang for providing me access to their vast bodies of knowledge compiled over years of experience in their respective fields. I would especially like to extend my thanks to my advisor, Zach Sharp, for continually pushing me to be a better version of myself while allowing me the freedom to satisfy my obsessive nature. His guidance and enthusiasm have been indispensable throughout this process.

I would also like to thank everyone at the Center for Stable Isotopes, including Viorel Atudorei, Karen Ziegler, Laura Burkemper, and Chris Anderson, for providing me with the guidance and know-how needed to operate and maintain the laser fluorination line and mass spectrometer used for this work. This research would not have been possible without the support, resources, and equipment provided by CSI. A big thank you to Oleg Maltsev for showing me the ropes when I first started analyzing samples. To Jordan Wostbrock, for her continued guidance and support in the world of triple oxygen isotopes, thank you. Thank you to Tony Gargano, my friend, office mate, and ever-present devil's advocate, who is always open to having ideas bounced off him.

Thank you to NASA, CAPTEM, and Lunar Samples Curation at the Johnson Space Center for providing us with the Apollo samples analyzed in this study. To everyone who sent us terrestrial samples to analyze, including Jane Selverstone, F. Trusdell, M. Perfit, V. S. Kamenetsky, L. S. Crumpler, K. A. Smart, S. Tappe, S. C. Kruckenberg, B. Oller, and L. D. Ashwal, thank you. Thank you, to my mother who has always been there to support me in what I do throughout the years. To my best friend, Rachelle Turnier, thank you for inspiring me to apply for graduate school and always being there for emotional support when the going got tough. And finally, thank you to the Grateful Dead, for providing the soundtrack that got me through those long nights in the lab.

**POST-IMPACT LIGHT VAPOR INCORPORATION DURING LUNAR FORMATION BASED ON TRIPLE OXYGEN ISOTOPES**

**by**

**Erick Jason Akio Cano**

**B.S., Geology, California State University, Long Beach, 2015**
**M.S., Earth and Planetary Sciences, University of New Mexico, 2018**

# ABSTRACT

Initial triple oxygen isotope analyses of lunar samples showed them to be indistinguishable from Earth, which led to numerous papers aimed at explaining the similarities. Recent high-precision analyses suggested either a subtle enrichment in $\Delta'^{17}O$ or virtually no difference between the Earth and Moon. Herein we expand on previous studies by correlating the triple oxygen isotope measurements with different lunar lithologies. We show that these data can be explained by mixing between a light vapor phase, generated during the Giant Impact, and the residual material from the proto-lunar impactor 'Theia'. There is a general decrease in $\Delta'^{17}O$ with the expected contribution from the "contaminating" vapor phase. Our data suggests that the sample which best preserves the lunar mantle has a $\Delta'^{17}O$ value of -0.030‰, giving us a minimum estimate for the lunar interior and the impactor Theia. The estimated Earth mantle value measured by this study is -0.052‰, suggesting a distinct difference between Earth and Moon.

# TABLE OF CONTENTS

# LIST OF FIGURES

# LIST OF TABLES

## INTRODUCTION & BACKGROUND

Earth's Moon is unique in that it is thought to have been formed from the debris of a large-scale collision between a partially formed proto-Earth and a smaller, Mars-sized proto-planet given the informal name 'Theia' (Hartmann and Davis, 1975; Cameron and Ward, 1976; Cameron and Benz, 1991; Cameron, 1997; Canup and Asphaug, 2001). In contrast, many of the other moons throughout the solar system are thought to have formed in conjunction with their planet from a shared accretion disk or originated as captured planetesimals. The Giant Impact Hypothesis, first proposed by two independent and contemporaneous studies (Hartmann and Davis, 1975; Cameron and Ward, 1976), is the currently favored explanation for the Moon's origin. This model was capable of accounting for the then recent observations from samples returned by the Apollo missions which included the Moon's lack of iron, depletion in volatiles, and enrichment in refractory elements, while avoiding most of the pitfalls of previous lunar origin theories. Early numerical simulations of planetary collisions generally supported the Giant Impact (e.g. Benz et al., 1986, 1987, 1989; Melosh and Kipp, 1989; Cameron and Benz, 1991) finding that a single large impact could produce (1) the initial angular momentum of the Earth-Moon system and (2) eject a sufficient amount of iron-depleted material into orbit to form the Moon. However, these classic collision models typically predicted that the Moon would have accreted from approximately 70-90% of the proto-lunar impactor Theia.

Having such a large portion of the Moon originate from Theia has proven to be a major issue for the Giant Impact Hypothesis because it has been historically observed that the Earth and Moon have nearly identical non-volatile isotope ratios (Dauphas et al.,

2014; Melosh, 2014; Stevenson and Halliday, 2014; Hauri et al., 2015). Looking specifically at the triple oxygen isotope system, analyses of lunar basalt samples have produced average values that are virtually indistinguishable from Earth (Wiechert et al., 2001; Spicuzza et al., 2007; Hallis et al., 2010; Young et al., 2016). This compositional conundrum of nearly identical oxygen isotope compositions for the Earth and Moon have led to numerous papers that seek to explain these similarities, all of which typically fall into one of the following categories. The simplest explanation is that proto-Earth and Theia initially had similar $\Delta'^{17}O$ values. If the idea of isotopic heterogeneity among differentiated bodies in the solar system holds true, the proto-Earth and Theia must have formed at similar heliocentric distances from the same isotopic reservoir (Wiechert et al., 2001; Mastrobuono-Battisti et al., 2015). It has also been proposed that some form of isotopic re-equilibration has occurred between the Earth and Moon post-impact, and the original isotopic heterogeneity present was lost (Pahlevan and Stevenson, 2007; Wang and Jacobsen, 2016; Lock et al., 2018). Alternatively, the canonical Giant Impact model may be incorrect, and the Moon may be the product of a more energetic, larger collision that allowed the Moon to accrete from a greater proportion of proto-Earth material (Reufer et al., 2012; Canup, 2012; Ćuk and Stewart, 2012).

The most recent high-precision oxygen isotope analyses are inconclusive as to whether the Earth and Moon have the same $\Delta'^{17}O$ composition. Herwartz *et al.* (2014) suggests that the Moon has a higher $\Delta'^{17}O$ value than the Earth by 12 ± 3 ppm (0.012‰). Young *et al.* (2016) and Greenwood *et al*. (2018) suggest smaller differences of −1 ± 5 ppm (-0.001 ‰) and 4 ± 3 ppm (0.004‰) respectively, demonstrating that there is practically no identifiable difference in $\Delta'^{17}O$ between the Earth and Moon. We expand

on the previous work by performing high-precision, whole-rock oxygen isotope analyses on a wide variety of lunar lithologies and mineral separates. We can demonstrate that the method of averaging together different lunar lithologies to produce a bulk lunar mantle value is flawed. There is real variation of the $\Delta'^{17}O$ value between different lunar lithologies that is likely due to differing degrees of incorporation of an isotopically anomalous silicate atmosphere immediately following the Giant Impact. The least contaminated materials, representative of the bulk Moon, show a distinct difference from Earth.

## RESULTS & DISCUSSION

Oxygen isotope analyses were performed at the Center for Stable Isotopes (CSI) using the standard laser fluorination technique (Sharp, 1990) with a modified $O_2$ purification process to obtain ultra-high precision results for $\Delta'^{17}O$ (see supplementary material for full methods). Our analytical precision, based on the repeated analysis of a San Carlos olivine internal standard (Table 1), is ±0.138‰ for $\delta^{18}O$ and ±0.004‰ for $\Delta'^{17}O$ ($n = 44$, 1σ SD). We measured a suite of lunar samples that included high- and low-Ti mare basalts, highland anorthosites, norites, and volcanic glasses as well as mineral separates from several of the aforementioned samples and others. A suite of terrestrial samples was also measured to determine the value of the bulk silicate Earth. These samples included dunite, numerous basaltic glasses from MORB and ocean island sources, and mineral separates from various peridotite samples. The full sample list for both suites is available in supplementary materials.

Averaging the $\Delta'^{17}O$ values obtained from our measurements of bulk lunar samples to determine the value for the bulk silicate Moon (BSM), as was done in

previous studies (e.g. Wiechert et al., 2001; Spicuzza et al., 2007; Hallis et al., 2010; Herwartz et al., 2014; Young et al., 2016; Greenwood et al., 2018), yields a $\Delta'^{17}O$ value of -0.049 ± 0.003‰ (2σ SEM n = 23) (Fig.1). The bulk silicate Earth (BSE) value obtained from averaging our measurements of the terrestrial suite of samples is -0.052 ± 0.002‰ (2σ SEM n = 22) (Fig.1), which would indicate that the Earth and Moon are practically indistinguishable with respect to $\Delta'^{17}O$, and based on these data alone, would be consistent with the findings of most previous studies (e.g. Wiechert et al., 2001; Spicuzza et al., 2007; Hallis et al., 2010; Young et al., 2016; Greenwood et al., 2018). What is noteworthy is the lunar samples have double the $\Delta'^{17}O$ variability (standard deviation of 0.0066‰), compared to Earth (standard deviation of 0.0037‰). Similar ranges for lunar sample $\Delta'^{17}O$ measurements have been seen in previous work, but this variation was within the limits imposed by their precision at the time (e.g. Wiechert et al., 2001; Spicuzza et al., 2007; Hallis et al., 2010). Given our precision for these $\Delta'^{17}O$ measurements and the diversity of our lunar sample suite, we are able to identify trends between the range in $\Delta'^{17}O$ values and other petrologic characteristics.

While the lunar mare basalts offer a first-order estimate of the isotopic composition of the lunar interior, they do not provide the complete story. This is apparent when the $\Delta'^{17}O$ values are considered by lithological type (Fig. 2) because distinct differences are seen between different rock types. Aside from several anomalous samples (explained in the supplementary material), the mare basalt samples and volcanic glasses show a trend of decreasing $\Delta'^{17}O$ values with increasing $TiO_2$ content (Fig. 3). The low-Ti basalts range between -0.037 and -0.047‰ and have an average of -0.042‰, while the High-Ti basalts range between -0.046 to -0.056‰ and have an average of -0.052‰. This

difference becomes even more apparent when comparing the lunar volcanic glasses, which represent examples of near primary values for their associated melts (Shearer and Papike, 1993; Shearer et al., 1996). The Apollo 15 very-low-Ti green glass and Apollo 17 high-Ti glass have $\Delta'^{17}O$ values of -0.030‰ and -0.049‰ respectively (Fig. 3). The isotopic heterogeneity seen between these types of samples does not appear to be caused by any type of mineral-specific isotope fractionation (e.g. Kohl et al., 2017). The $\Delta'^{17}O$ values of the major Ti-bearing phase, ilmenite, is the same as the bulk rock, and calculated $\theta$ values between pyroxene and plagioclase in a high-Ti lunar basalt (~0.537) and 'pristine' terrestrial mafic rocks (~0.522 to ~0.530) are consistent with high-temperature equilibrium (see supplementary material).

Instead, we propose that the regular variation seen in the lunar $\Delta'^{17}O$ values is caused by the mixing of two different isotopic reservoirs. The first is the deep lunar mantle material, that retains the original value of the proto-lunar impactor, and the second is a low $\Delta'^{17}O$ component formed from the incorporation of the condensed silicate vapor atmosphere immediately following the Giant Impact. As suggested by previous work (Canup, 2004; Pahlevan and Stevenson, 2007), a silicate vapor envelope is thought to have formed around a molten Moon post-Giant Impact. Experiments have shown that there is a large $\Delta'^{17}O$ mass independent fractionation during condensation of $SiO_2$ from SiO gas in the presence of hydrogen (Kimura et al., 2007; Chakraborty et al., 2013). The condensing $SiO_2$ is strongly enriched in $^{17}O$ while the residual vapor can attain extremely low $\Delta'^{17}O$ values. It can therefore be expected that the early-formed condensate would be well-mixed back into the lunar magma ocean (LMO) during the waning stages of condensation following the Giant Impact, while low $\Delta'^{17}O$ material is delivered to the

surface of the Moon. This isotopically light, late contribution would then be incorporated into the outermost portion of the LMO. Based on dynamic models for LMO convection (Spera, 1992; Elkins-Tanton et al., 2011), this light signature contaminated material could remain sequestered in the viscous surface layer of a stratified magma ocean, unmixed into the deeper portions of the LMO. The exceptionally light $\Delta'^{17}O$ values we see in some mineral separates from troctolitic anorthosites and regolith breccias measured in this study can be explained by this surface layer contamination. Furthermore, we predict that any samples that may have assimilated or mixed with this surface layer contamination may have their $\Delta'^{17}O$ lowered to some degree by this interaction.

To understand how this light signature is then incorporated into different lunar lithologies, it is necessary to further investigate their petrogenesis. The early-formed crustal samples, including anorthosite and the Mg-suite rocks or components generally have the lowest $\Delta'^{17}O$ values, consistent with the largest degree of late, light vapor incorporation. The other endmember is the deeply sourced very-low-Ti green glass (sample 15426) which presumably has the lowest amount of crustal contamination and the highest $\Delta'^{17}O$ value of -0.030‰. Such a conclusion is supported by the high water contents for the green glass (Saal et al., 2008; Hauri et al., 2015) which is consistent with retention of primary lunar volatiles at depth. It is therefore our minimum estimate for the non-contaminated Theia component.

Crystallization of the LMO produced cumulates with a large variety of compositions which are thought to be sources for the later periods of lunar basaltic magmatism (Shearer et al., 2006). Formation of the high- and low-Ti mare basalts involved the mixing of at least two lunar reservoirs with different oxygen isotope

compositions. One of these reservoirs is the deeply sourced lunar mantle cumulates that most closely preserve the proto-lunar values of Theia, while the other is sourced in part from the near-surface where the light vapor contamination has occurred. The initial crystallization of the LMO produced olivine and pyroxene cumulates that settled towards the base of the LMO and preserve the proto-lunar impactor $\Delta'^{17}O$ signature. The Ti-rich pyroxene + ilmenite ± olivine cumulates formed in the final stages of LMO crystallization are depleted in plagioclase since they formed from the residual melt left over after anorthosite removal to the crust (Ringwood and Kesson, 1976; Kesson and Ringwood, 1976). They should have the same light vapor contaminated $\Delta'^{17}O$ values seen in crustal samples. These low $\Delta'^{17}O$, Ti-rich cumulates would become gravitationally unstable in relation to their surrounding materials due to the dense ilmenite they contain (Ringwood and Kesson, 1976; Kesson and Ringwood, 1976). The dense ilmenite-bearing cumulates, having formed near the top of the cumulate pile, forced the mantle to undergo overturn in order to reach a gravitationally stable state. Through the overturn process, the ilmenite-bearing cumulates sank down into the underlying olivine + pyroxene cumulates where they combined and remelted, forming hybridized magmas. Partial melting of these magmas, which were hybridized to varying degrees, are thought to be the source for the high-Ti mare basalts and possibly the entire spectrum of mare basalts (Ringwood and Kesson, 1976; Kesson and Ringwood, 1976; Shearer and Papike, 1993; Hess and Parmentier, 1995; Zhong et al., 2000).

As ilmenite-bearing cumulates combine with the deeper olivine and pyroxene cumulates partial melting occurs, forming hybrid magmas that contain a large percentage of high-Ti material and subsequently a larger contribution of light vapor contaminated

material. The larger proportion of contaminated material, with light $\Delta'^{17}O$ values combines with the olivine and pyroxene cumulates, which have retained the proto-lunar signature (-0.030‰). High-Ti basalts produced from these magmas are imbued with the higher $TiO_2$ compositions and larger negative Eu anomalies associated with the ilmenite-bearing cumulates and adopt $\Delta'^{17}O$ values ranging from -0.047 to -0.056‰. Coincidentally, these high-Ti basalts average to around the same $\Delta'^{17}O$ value as the BSE.

The low-Ti basalts, have a smaller contribution from the light vapor contaminated, ilmenite-bearing cumulate component, hence the lower $TiO_2$ content and smaller negative Eu anomalies. Since there was a larger contribution from the deep olivine and pyroxene cumulates with the higher $\Delta'^{17}O$ signature (-0.030‰), low-Ti hybrid magmas were formed that retained more of the uncontaminated proto-lunar signature and thus have $\Delta'^{17}O$ values ranging from -0.036 to -0.047‰. Therefore, the low-Ti basalts, which possess lower amounts of ilmenite and have the smaller negative Eu anomalies, can generally be considered less contaminated by the light vapor component and more representative of lunar bulk silicate mantle.

The same relationship is evidenced more clearly in the volcanic lunar glasses that were measured for this study. As mentioned previously, the Apollo 15 very-low-Ti green glass had the highest measured $\Delta'^{17}O$ value at -0.030‰ and the lowest $TiO_2$ content. They are also water-rich (Saal et al., 2008; Hauri et al., 2015), suggesting less volatile loss during the formation of the Moon (Canup et al., 2015; Lock et al., 2018). Based on the very low Ti content it is likely that the Apollo 15 green glass represents the material that is the least contaminated by any light vapor component and is most representative of Theia isotopic oxygen values, from the sample suite measured. In contrast, the Apollo 17

high-Ti glass has both $TiO_2$ content and a $\Delta'^{17}O$ value that fall in the average range for high-Ti basalt. Since the lunar volcanic glasses are thought to represent examples of near primary values for their associated melts (Shearer and Papike, 1993; Shearer et al., 1996), this correlation further strengthens the argument that the same process which incorporated Ti into these samples may have also decreased the $\Delta'^{17}O$ values.

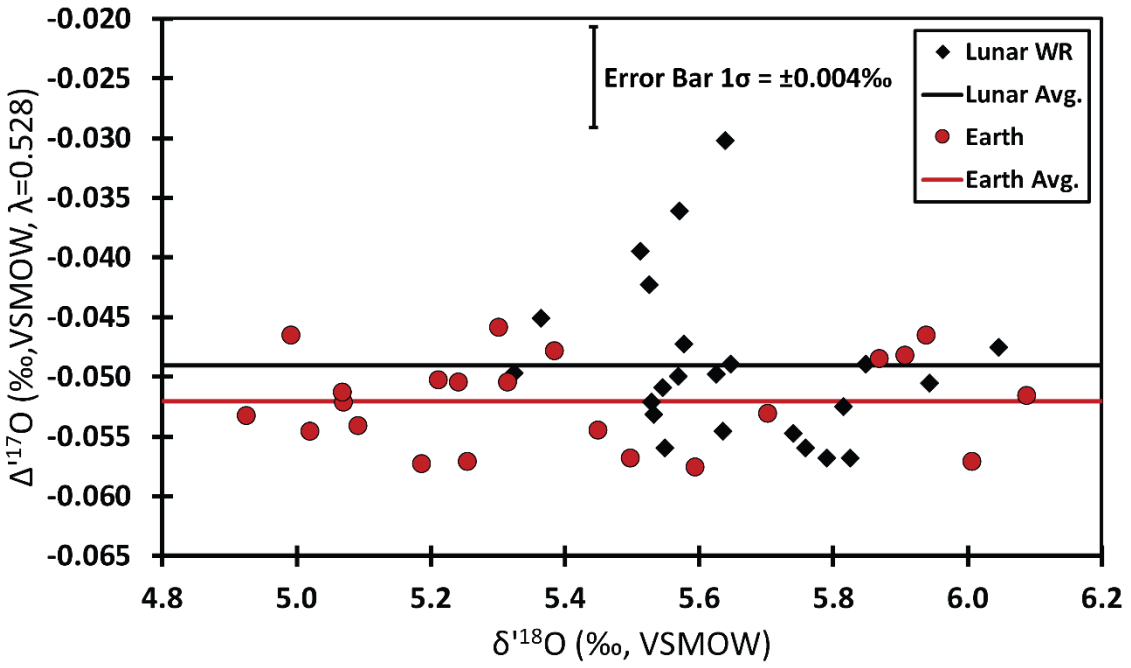


**Fig. 1. Plot of $\Delta'^{17}O$ versus $\delta'^{18}O$ for lunar and terrestrial samples.** Lunar samples are represented by the black diamonds, and terrestrial samples are represented by the red circles. Only lunar whole-rock (WR) measurements are plotted (no lunar mineral separates). A combination of whole-rock and mafic mineral separates, which were used for the BSE calculation, are plotted for the terrestrial samples. Error bar represents 1σ standard deviation. The black line and red line indicate the mean values for the lunar samples and terrestrial samples respectively. The lunar samples display a much larger range of $\Delta'^{17}O$ variability with a standard deviation of 0.0066‰ (1σ), nearly twice that of the Earth's 0.0036‰ (1σ) standard deviation.

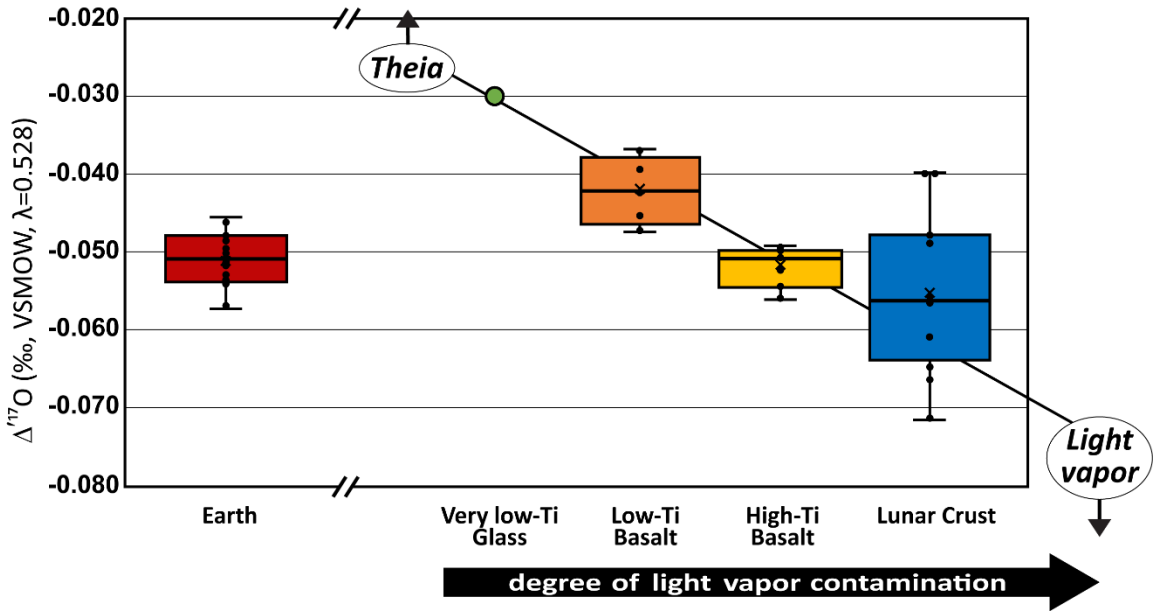


**Fig. 2. Box and whisker plot showing the $\Delta'^{17}O$ values for the different lunar lithologies and Earth.** A clear trend can be seen where $\Delta'^{17}O$ values decrease with an increasing degree of contamination from the light vapor. The very low-Ti volcanic glass has the least amount of contamination and therefore represents the closest approximation of original Theia value which is at least -0.030‰ but could be higher. This trend continues through the low-Ti basalts, high-Ti basalts and lunar crustal lithologies. The bar within the boxes indicate the median value, and the X denotes the mean value. Additionally, it should be noted that the high-Ti basalts occupy nearly the same $\Delta'^{17}O$ range as the bulk silicate Earth. (Note: Whole-rock measurement values were used for the low- and high-Ti basalt data on this plot, however, due to the small quantity of lunar crust whole-rock samples in our selection, it was necessary to supplement those data with mineral separate data. This is in part responsible for the large variation seen in the lunar crust samples, see supplemental.)

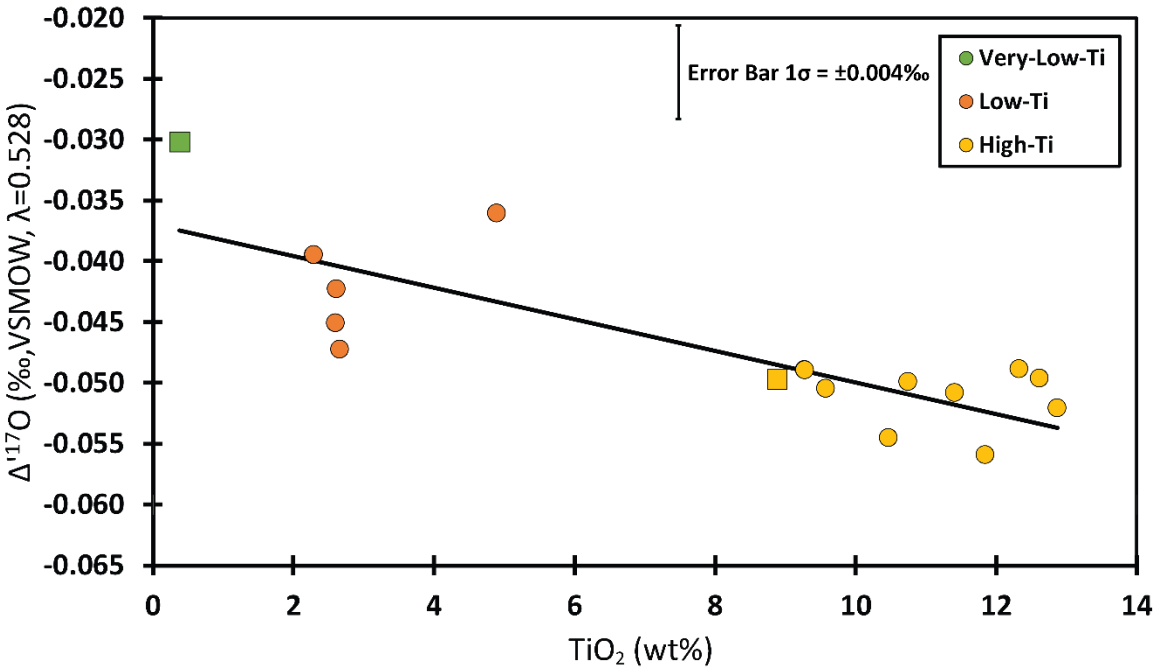


**Fig. 3. Plot of $\Delta'^{17}O$ versus $TiO_2$ content for high- and low-Ti lunar mare basalts and volcanic glasses.** High- and low-Ti basalts are represented by orange and yellow circles respectively. Error bar denotes 1σ standard deviation. Lunar mare basalts show a trend of decreasing $\Delta'^{17}O$ values with increasing $TiO_2$ content. The square data points indicate that the sample was a volcanic glass, which demonstrate the same trend as the high- and low-Ti basalts. The $TiO_2$ values used for this plot are averaged from the major oxide data found in the Lunar Sample Compendium and the references found therein)

## CONCLUSION

The above argument is consistent with the clear trend of decreasing $\Delta'^{17}O$ values with an increasing degree of contamination ranging from the least contaminated very low-Ti green glass through the lunar crustal material. Since the best-preserved representation of the lunar mantle has a $\Delta'^{17}O$ value that is about -0.030‰, we suggest that the proto-lunar impactor Theia had a $\Delta'^{17}O$ value that was at minimum -0.030‰, making the Moon distinctly different from the estimated Earth mantle value of -0.051‰. Therefore, if the heterogeneity of terrestrial bodies in the inner solar system trends towards higher $\Delta'^{17}O$ values with heliocentric distance, Theia would have an origin further out from the Sun relative to Earth. It should also be noted that the high-Ti lunar basalts occupy nearly the same $\Delta'^{17}O$ range as terrestrial samples representing the BSE (Fig. 2), and we attribute this coincidence to be a product of the mixing between the two reservoirs. The large majority of samples analyzed in the present and previous studies are from Apollo 17 high-Ti ilmenite basalts, so it is no surprise that when averaged they produce $\Delta'^{17}O$ values very similar to Earth.

Lunar samples show a variation that is nearly twice that which is seen in the $\Delta'^{17}O$ values for Earth's mantle (Fig. 1). This large range can be explained by the mixing of a proto-lunar Theia component preserved in the lunar interior and a vapor contaminated component from interaction with surface material. The preservation of this variation supports the idea that the LMO was not entirely homogenized (Spera, 1992; Elkins-Tanton et al., 2011), and lunar mare basalts cannot be averaged to estimate a lunar mantle value. By this rationale, the disagreement between previous high-precision studies is, in part, the result of sample selection. Differences in $\Delta'^{17}O$, or lack-there-of, between the

Earth and Moon determined by each study, based on lunar basalt analysis, is wholly dependent on the samples used and does not provide a reliable estimation of the BSM.

# APPENDICES

## APPENDIX I: Analytical Methods

Oxygen isotope analyses were performed at the Center for Stable Isotopes' (CSI) laboratory at UNM using the standard laser fluorination technique (Sharp, 1990) with a modified $O_2$ purification process to obtain ultra-high precision results for $\Delta'^{17}O$. For whole rock analysis, sample chips were selected that were as homogenous as possible and representative of the larger sample's overall composition. Fragments of samples were used as opposed to powdered samples to minimize the amount of water that could be adsorbed to the surface. Samples for mineral separate analysis were crushed, sieved, and the required mineral grains were separated. Mineral separation was performed using a combination of heavy liquid separation with bromoform and methylene iodide, magnetic separation using a Frantz Isodynamic Magnetic Separator, and hand picking. Samples were loaded into a 44-well nickel sample plate with approximately 2 mg of sample in each well. San Carlos olivine laboratory standards were loaded into the plate as well in order to calibrate the runs performed each day. The samples were loaded using an alternating checkerboard pattern, skipping every other sample hole, to avoid any contamination of other samples should the $CO_2$ laser eject any grains during the fluorination process. The sample plate was loaded into the fluorination chamber and placed under vacuum 24-48 hours prior to sample analysis. Additionally, a halogen lamp was used to warm the sample plate and chamber over this period, to drive off any surficial $H_2O$ that may have been introduced during the sample preparation and loading. This lamp heating step combined with the use of non-powdered samples and prefluorination should be sufficient to eliminate any adsorbed water issues that could affect triple oxygen isotope analyses, as mentioned in Young *et al.* (2016).

$BrF_5$ gas was used to prefluorinate the samples prior to analysis, allowing any remaining surface contamination or $H_2O$ to react and be removed. This was performed by introducing 120 mbar of $BrF_5$ to the sample chamber and allowing it to react for one hour at room temperature. Any byproducts produced by this prefluorination reaction were reacted with a NaCl trap and removed through the waste portion of the oxygen fluorination line.

The extraction of $O_2$ gas from the samples was performed by introducing 100 mbar of $BrF_5$ to the sample chamber, and heating the sample using a $CO_2$ laser. Laser power was gradually increased, and the spot diameter of the beam was simultaneously decreased in order to completely react the sample with the $BrF_5$ gas. In addition to the $O_2$ produced in the reaction, other products of silicates reacting in a $BrF_5$ atmosphere can include $SiF_4$, $BrF_3$, $Br_2$, and $F_2$ (Kusakabe et al., 2004). These products along with any others and excess $BrF_5$ were frozen in a liquid nitrogen cold trap following the fluorination reaction. The $O_2$ gas was then passed through three additional liquid nitrogen cryogenic traps and a heated NaCl trap for further purification. The oxygen was then collected using a 5 Å molecular sieve trap submerged in liquid nitrogen. By lowering the temperature of the molecular sieve zeolites, they are able to rapidly adsorb the purified oxygen. After collection of the oxygen, the molecular sieve trap was heated, releasing the oxygen into a stream of helium carrier gas which passes it through a 6 ft x 1/8 in 60/80 Mol Sieve 13X gas chromatograph (GC) column. The addition of the GC to the extraction line allows us to ensure that the $O_2$ sample entering the mass spectrometer is as pure as possible. A source of systematic error encountered in high precision $\Delta'^{17}O$ measurements is the production of $NF_3$. Trace quantities of $NF_3$ can be produced as a

byproduct of fluorination. Inside the mass spectrometer, $NF_3^+$ can fragment forming $NF^+$, which interferes with the mass signal for $^{17}O$ (Herwartz et al., 2014; Young et al., 2016). By using the GC we're able to ensure that the $O_2$ is separated from $NF_3$ and any other problematic gasses, which lends to the accuracy of the $\delta^{17}O$ measurements we can obtain.

After refinement in the GC, the purified $O_2$ gas was collected in a second molecular sieve trap immersed in liquid nitrogen. This trap is attached to the sample inlet of a Thermo Fisher MAT 253 Isotope Ratio Mass Spectrometer. Excess helium was pumped away through the mass spectrometer's vacuum pumps while the oxygen remained adsorbed in the molecular sieve. The trap was then heated, and the $O_2$ gas was released into the mass spectrometer bellow. In dual inlet configuration, analysis of $O_2$ from each sample was run against the CSI laboratory's $O_2$ reference gas standard. Each sample run consisted of 40 iterations; in which, each iteration included a 26 second collection time for the reference and sample gas separated by a 15 second delay. These long collection times allow us to obtain reproducible, high-precision $\Delta'^{17}O$ values.

The analyses were recorded using the Isodat 3.0 acquisition software. Iterations with values outside a 1σ standard deviation were omitted automatically by the program, and an average of all iterations was used for the determination of $\delta^{17}O$ and $\delta^{18}O$ values for each run. These values were linearized using Equation 2, and Equation 7 is used to determine the $\Delta'^{17}O$ value for each sample with respect to $\lambda$=0.528.

Oxygen isotope measurements of rocks, minerals, and water are typically reported relative to VSMOW. We maintain the use of the traditional standard for oxygen isotope analyses, Vienna Standard Mean Ocean Water (VSMOW), and report all $\delta'^{17}O$, $\delta'^{18}O$, and $\Delta'^{17}O$ values with respect to VSMOW. Others argue against the use of VSMOW as the

reference for $\Delta'^{17}O$ (Young et al., 2016) due to the technically challenging aspect of fluorinating water, and the possibility for systematic errors introduced by using different analytical procedures to measure rocks and water samples. However, we are capable of and have measured VSMOW on the same fluorination system used for our rock measurements (Sharp et al., 2016). Therefore, our San Carlos olivine laboratory standard and reference $O_2$ gas has been recalibrated against $O_2$ obtained through the direct fluorination of VSMOW, which was performed on the same system used to obtain these data. Our analytical precision, based on the repeated analysis of a San Carlos olivine internal standard (Table 1), is ±0.138‰ for $\delta^{18}O$ and ±0.004‰ for $\Delta'^{17}O$ ($n$ = 44, 1σ SD).

**Table 1. Oxygen isotope data for San Carlos olivine**

**San Carlos Olivine**

| Sample | $\delta^{17}O$ | $\delta^{18}O$ | $\delta'^{17}O$ | $\delta'^{18}O$ | $\Delta'^{17}O$ |
|---|---|---|---|---|---|
| 1 | 2.641 | 5.103 | 2.637 | 5.090 | -0.050 |
| 2 | 2.814 | 5.422 | 2.810 | 5.408 | -0.046 |
| 3 | 2.744 | 5.286 | 2.740 | 5.272 | -0.044 |
| 4 | 2.723 | 5.256 | 2.719 | 5.242 | -0.049 |
| 5 | 2.689 | 5.197 | 2.685 | 5.183 | -0.052 |
| 6 | 2.727 | 5.263 | 2.723 | 5.249 | -0.048 |
| 7 | 2.707 | 5.224 | 2.703 | 5.210 | -0.048 |
| 8 | 2.664 | 5.143 | 2.660 | 5.129 | -0.048 |
| 9 | 2.704 | 5.222 | 2.700 | 5.208 | -0.050 |
| 10 | 2.723 | 5.261 | 2.719 | 5.247 | -0.051 |
| 11 | 2.697 | 5.210 | 2.693 | 5.196 | -0.051 |

**Table 1. Continued**

| Sample | $\delta^{17}O$ | $\delta^{18}O$ | $\delta'^{17}O$ | $\delta'^{18}O$ | $\Delta'^{17}O$ |
|---|---|---|---|---|---|
| 12 | 2.628 | 5.074 | 2.624 | 5.061 | -0.048 |
| 13 | 2.626 | 5.083 | 2.622 | 5.070 | -0.055 |
| 14 | 2.496 | 4.841 | 2.493 | 4.829 | -0.057 |
| 15 | 2.615 | 5.044 | 2.611 | 5.031 | -0.045 |
| 16 | 2.639 | 5.123 | 2.635 | 5.109 | -0.063 |
| 17 | 2.760 | 5.328 | 2.756 | 5.313 | -0.050 |
| 18 | 2.591 | 5.020 | 2.587 | 5.007 | -0.056 |
| 19 | 2.632 | 5.083 | 2.628 | 5.070 | -0.049 |
| 20 | 2.746 | 5.301 | 2.742 | 5.287 | -0.049 |
| 21 | 2.736 | 5.282 | 2.732 | 5.268 | -0.049 |
| 22 | 2.690 | 5.205 | 2.686 | 5.191 | -0.055 |
| 23 | 2.829 | 5.469 | 2.825 | 5.455 | -0.055 |
| 24 | 2.716 | 5.240 | 2.712 | 5.226 | -0.047 |
| 25 | 2.656 | 5.132 | 2.652 | 5.118 | -0.050 |
| 26 | 2.733 | 5.278 | 2.729 | 5.264 | -0.050 |
| 27 | 2.577 | 4.982 | 2.573 | 4.969 | -0.050 |
| 28 | 2.749 | 5.300 | 2.745 | 5.286 | -0.046 |
| 29 | 2.639 | 5.103 | 2.635 | 5.090 | -0.052 |
| 30 | 2.789 | 5.382 | 2.785 | 5.368 | -0.050 |
| 31 | 2.809 | 5.413 | 2.805 | 5.399 | -0.046 |
| 32 | 2.772 | 5.345 | 2.768 | 5.330 | -0.047 |
| 33 | 2.739 | 5.288 | 2.735 | 5.274 | -0.050 |
| 34 | 2.740 | 5.309 | 2.736 | 5.294 | -0.060 |
| 35 | 2.675 | 5.165 | 2.671 | 5.151 | -0.049 |
| 36 | 2.551 | 4.941 | 2.547 | 4.928 | -0.055 |
| 37 | 2.809 | 5.399 | 2.805 | 5.385 | -0.039 |
| 38 | 2.727 | 5.264 | 2.723 | 5.250 | -0.049 |
| 39 | 2.767 | 5.335 | 2.763 | 5.320 | -0.046 |
| 40 | 2.796 | 5.390 | 2.792 | 5.376 | -0.047 |
| 41 | 2.805 | 5.427 | 2.801 | 5.413 | -0.057 |
| 42 | 2.710 | 5.243 | 2.706 | 5.229 | -0.055 |
| 43 | 2.765 | 5.347 | 2.761 | 5.332 | -0.055 |
| 44 | 2.724 | 5.253 | 2.720 | 5.239 | -0.046 |
| | | | | | |
| Average | 2.706 | 5.226 | 2.702 | 5.213 | -0.050 |
| SD (1σ) | 0.074 | 0.138 | 0.074 | 0.137 | 0.004 |
| SEM (1σ) | 0.011 | 0.021 | 0.011 | 0.021 | 0.001 |

## APPENDIX II: Sample Descriptions

### *Lunar sample descriptions*

The following lunar sample descriptions are abbreviated from the Lunar Sample Compendium (Meyer, 2012) and the references found therein.

10017 – A fine- to medium-grained, vesicular, ilmenite basalt categorized as a high-K variety that shows a lack of any alteration and has a glassy mesostasis. It is composed primarily of clinopyroxene (~50%), plagioclase (~25%), and ilmenite (~15%).

10020 – A fine-grained, vuggy, ilmenite basalt categorized as a low-K variety and covered in micrometeorite craters. It is composed primarily of olivine (~6%), pyroxene (~45%), plagioclase (~30%), and ilmenite (~15%). The olivine phenocrysts are commonly clumped in groups and tend to be much larger than the other major minerals; this may suggest that the olivine formed prior to extrusion.

10044 – A coarse-grained, vuggy, porphyritic ilmenite basalt categorized as a low-K variety. It consists of pyroxene phenocrysts (45%) set in a matrix of plagioclase tablets (~35%) and ilmenite (~13%). There is essentially no olivine, and the pyroxene is chemically zoned.

12002 – A medium-grained, porphyritic olivine basalt with a glassy mesostasis containing irregularly shaped vugs. The composition is primarily olivine (~17%) and clinopyroxene (~49%) phenocrysts set in a matrix of intergrown pyroxene and plagioclase (~16%). The phenocrysts frequently have crystallized melt inclusions, which indicates that the phenocrysts formed as skeletal crystals that encapsulated the melt. Some of the plagioclase have hollow cores and are compositionally reverse zoned.

12018 – A medium-grained olivine basalt that displays virtually no shock-metamorphism or deformation and has a relatively high mafic mineral content. It is primarily composed larger olivine (~20%) and pyroxene (~60%) crystals set in a variolitic matrix containing plagioclase (~17%) and shows an apparent surface "encrustation".

12054 – A medium-grained, equigranular, glass-coated ilmenite basalt. The glass coating did not form *in situ*, but it is a shock feature deposited as an "impact melt splash" derived from a similar basalt and has thermally modified the sample along its contact. It is composed primarily of intergrown plagioclase (~29%) and pyroxene (~62%), suggesting cotectic crystallization. It also contains olivine (~11%) and elongate ilmenite (~5%).

12063 – A medium-grained, porphyritic ilmenite basalt containing phenocrysts of olivine (~3-9%) and pyroxene (~64%) set in a matrix of intergrown plagioclase (~25%), pyroxene, and opaque minerals, including ilmenite (~5%). The interstitial areas in the matrix are filled with glassy mesostasis and contains vermicular intergrowths of glass and clinopyroxene.

14053 – A medium-grained, ophitic aluminous mare basalt with large, zoned pyroxene (~50%) grains surrounding plagioclase (~40%) laths. One side of the sample is rounded and pitted with microcraters while the other side was flat and has attached breccia material, indicating that this basalt may have been a clast in a nearby breccia boulder.

15016 – A medium-grained, highly-vesicular olivine-normative basalt in which vesicles make up about 50% of the volume. It is primarily composed of phenocrysts of zoned pyroxene (~63%) and olivine (~8%) that are set in a matrix of intergrown pyroxene and plagioclase (~22%).

15426 – A fine-grained, extremely friable greenish colored regolith clod containing plagioclase, mafic silicates, small rock clasts, and pyroclastic green glass.

15535 – A fine- to medium-grained olivine-normative basalt. It is primarily composed of small, equant olivine (~10%) and pyroxene (~55%) crystals enclosed in poikilitic plagioclase (~30%).

15556 – A fine-grained, highly-vesicular olivine-normative basalt in which vesicles make up as much as 50% of the volume, and the mesostasis contains glass, silica, troilite, and grains of iron. The composition is primarily pyroxene (~55%) and plagioclase (~35%) with small amounts of ilmenite (2%) and olivine (<1%).

60016 – A friable, polymict, "ancient" regolith breccia containing light and dark clasts contained in a light grey matrix. The lithic lasts include Cataclastic and recrystallized anorthosite, impact melt, noritic anorthosite, dark matrix aphanitic melts, and glass fragments.

62237 – A chalky, white troctolitic anorthosite that is classified into the group of lunar ferroan anorthosites. It is claimed to be "chemically pristine," but has been crushed, forming a cataclastic texture in some places. Relic clasts of the original coarse-grained igneous texture can be seen, and it has an abundant amount of mafic minerals. It is primarily composed of olivine (~15%) and plagioclase (~85%) with very minor amounts of pyroxene.

70215 – A fine-grained, dense, porphyritic mare basalt that contains a high abundance of ilmenite (~13%) which sometimes occur within small vugs. It is composed

of phenocrysts of olivine (~7%) and ilmenite set in a groundmass of plagioclase (~20%) and pyroxene (~50%).

70255 – A fine-grained, blocky, subangular ilmenite basalt that is considered to be Ti-rich. It contains both olivine (~5%) and silica (~1.6%) which indicates that it likely crystallized rapidly. It is primarily composed of pyroxene (~47%), plagioclase (~15%), and opaques (~31%), which includes ilmenite.

71135 – A fine-grained, vesicular ilmenite basalt that contains large sawtooth ilmenite (~25%) needles in a matrix of intergrown plagioclase (~20%) and pyroxene (~50%).

71546 – An olivine-microporphritic ilmenite basalt that has variable grain sizes from fine-grained in some areas to coarser, granular areas. It is primarily composed of large pyroxene (~48%) grains that enclose ilmenite (~17%) and plagioclase (~28%) with a minor amount of olivine (~3%).

74220 – An orange soil sample or clod that is nearly pure orange pyroclastic glass with some ancient mare soil. A large portion of the orange glass devitrified to a black color due to fine needles of olivine and ilmenite feathers, but it is compositionally the same as the orange glass.

74275 – A fine-grained ilmenite basalt that contains olivine megacrysts, vesicles, vugs and has a significant amount of armalcolite. The composition is primarily olivine (~15%), pyroxene (~35%), plagioclase (~17%), and opaque minerals (~32%), which includes armalcolite rimmed with ilmenite. Pyroxene rims can be found on some olivine phenocrysts, and the mesostasis contains minor iron metal and troilite blebs.

75035 – A medium-grained, subophitic ilmenite basalt that slightly more aluminous and less Ti rich than other Apollo 17 basalts. It is more texturally similar to Apollo 11 basalts and contains laths of plagioclase (~32%) surrounded by pyroxene (~45%). Large ilmenite (~15%) laths penetrate both the plagioclase and pyroxene, indicating that it was likely the first to crystallize from the melt.

76335 – A very friable cataclastic magnesian anorthosite that is highly shocked, but apparently chemically pristine. It was returned as a number of fragments, and it is unknown if it is composed of all one rock, or different rock fragments that had formed a breccia. One fragment was reported to contain primarily plagioclase (~88%) and olivine (~12%), however another fragment was reported to contain orthopyroxene, merrillite, and chromite as well.

76535 – A coarse-grained, pristine, plutonic troctolite that is very friable and has not been damaged by shock events. It is primarily composed of coarse olivine (~36%) and plagioclase (~59%) with minor amounts of orthopyroxene (~5%). The sample displays evidence of extensive annealing and re-equilibration. The coarse grains have curved grain boundaries and a large amount of 120° junctions due to grain coarsening during annealing. It is considered an end member of the Mg troctolite suite of lunar highland rocks.

77215 – A friable cataclastic norite that is probably a brecciated pigeionite-anorthite cumulate, however the pigeonite has inverted to orthopyroxene with an augite exsolution. The sample was possibly a pristine norite that has been shocked and crushed. It is primarily composed of plagioclase (~54%) and orthopyroxene (~41%) and has trace amounts of troilite, ilmenite, clinopyroxene, silica, and K-feldspar. Upon return the breccia

broke into a number of pieces, some of which have small zones of unbrecciated norite, however most of the lithic clasts have been granulated or smeared to form schlieren.

78235 – A heavily-shocked norite with a glass coating and glass veins that likely originated as a cumulate. It is primarily composed of cumulus orthopyroxene and plagioclase which are both partially shattered. Much of the plagioclase has been converted to maskelynite, which indicates a shock pressure between 300 and 500 kbar. The glass coating may indicate that the sample had been a "bomb", and the presence of the glass veins could indicate that the rock experienced pressures in excess of 500 kbar. It is considered an end member of the Mg norite suite of lunar highland rocks.

***Terrestrial sample descriptions***

KE58-2842F – A Hawaiian basalt sample from Shelly pahoehoe, Royal Gardens. The sample was collected while still molten and quenched in distilled water (collected by F. Trusdell, June 4, 2009) (Sharp et al., 2013).

ALV2772-1 & ALV2746-12 – MORB glass samples collected at 9°N off-axis of the fast-spreading East Pacific Rise. The samples are optically and chemically pristine and free of any seawater alteration and were collected by Mike Perfit using the Alvin submersible (Sharp et al., 2007).

MAQ-25637, G882b & 47979 – Basaltic glasses are from Macquarie Island (54°30′S, 158°56′E) which constitutes an above sea-level exposure of the Macquarie Ridge. The ridge contains tholeiitic MORB-like basalt and marks the boundary between the Australia and Pacific plates. The glasses occur as quenched rims of basaltic pillow lavas as well as fragments in hyaloclastite breccias, the latter of which are glass lapilli, glassy and crystalline pillow fragments. Olivine microphenocrysts with trapped spinel are common,

but only constitute <5% of the total volume. Some glasses contain spinel and plagioclase laths, however no clinopyroxene were found. Olivine and plagioclase microphenocrysts show no indication of resorption or textural disequilibrium. Samples were selected avoiding areas where alteration had occurred or where microphenocrysts were observed, and they represent near-primitive compositions, as defined by Mg number and incompatible element contents (Kamenetsky et al., 2000).

Dunite – A dunite sample from the Addie Quarry within the Webster-Addie ultramafic ring, Jackson County, North Carolina. It contains about 90% or more medium- to coarse grained olivine and minor amounts of accessory minerals. Most grains have no inclusions, however chromite is occasionally present along cleavage traces (Miller, 1953).

TPS-03 & 02 – Tholeiite basalt samples from the olivine-bearing Thumb Point sill in Victoria Land, Antarctica. Chemical and mineral modal variation within the sill indicates *in situ* variation in which olivine and pyroxene have accumulated towards the bottom by gravitational settling (Gunn, 1966). It is primarily composed of olivine (~1-10%), pyroxene (~25-45%), plagioclase (~40-60%), and glassy mesostasis (~2-30%). The pyroxene and plagioclase vary inversely with the amount of mesostasis material throughout the sill, and the olivine is found only within the zone that ends 125 m from the base of the sill (Gunn, 1966; Wilhelm and Wörner, 1996)

Mesa Chivato & Grants Ridge basalts – These two basalts are associated with and located within the Mount Taylor volcanic field. Both samples contained phenocrysts and megacrysts of olivine and plagioclase. The Mesa Chivato basalt comes from a late, porphyritic alkali basalt found in El Dado Canyon, Northeast of Mount Taylor. It is primarily composed of plagioclase (~35-55%), orthoclase (~9%), olivine (~15%), and

pyroxene (~15-20%). Megacrysts from this sample lack compositional zoning and rounded or corroded rims that typically occur in low-pressure phenocrysts, so it is conceivable that they may have been entrained from cumulates of preceding suites (Crumpler, 1980). The Grants Ridge basalt is from a basaltic plug located in East Grants Ridge, to the West of Mount Taylor. These basalts are composed primarily of labradorite (~30%), olivine (~5-10%), augite (~10%), and magnetite (~5%) set in a cryptocrystalline and glassy groundmass (Hunt, 1938).

ST15-01A – A coarse-grained, granular garnet peridotite xenolith from kimberlite pipes in Kimberly, South Africa. The sample has an equigranular texture and slightly curved grain boundaries. It is primarily composed of coarse-grained olivine (~70%), orthopyroxene (~23%), garnet (~5%), and clinopyroxene (~2%). It shows no visible evidence of extensive metasomatism but have some serpentine alteration along grain boundaries (Katayama et al., 2009).

Gabbro - A medium-grained gabbro intrusion from the Duluth gabbro complex near Duluth, Minnesota. It is primarily composed of plagioclase tablets (~42%), elongate grains of olivine (~10%), and pyroxene (~46%) with minor interstitial magnetite-ilmenite (~1%), and none of the minerals appear to be significantly altered (Taylor, 1964; Phinney, 1969).

Finero peridotite – A coarse-grained phlogopite-peridotite from Finero in the Italian Western Alps. It is primarily composed of olivine (~40-65%), orthopyroxene (~25%), and clinopyroxene (~10%), with opaque minerals, spinel, hornblende, and phlogopite in varying amounts making up the remaining volume. Some olivine grains have been mylonitized or show plastic deformation, and both pyroxene and olivine show evidence for some recrystallization through annealing (Ernst, 1978).

Antarctic peridotite – A coarse-grained, granular, spinel-bearing peridotite xenolith from the Demas Bluff region of the Fosdick Mountains in Marie Byrd Land volcanic province of West Antarctica. It is primarily composed of olivine, orthopyroxene, clinopyroxene, and spinel, and all major mineral phases are compositionally Mg-rich with characteristics typical for subcontinental mantle xenoliths (Chatzaras et al., 2016).

Ferrel Seamount peridotite – A coarse-grained peridotite xenolith from the North flank of the Ferrel Seamount (29°33.9′N, 117°15.6′W). Geochemical data suggests that these xenolyths represent abyssal peridotites and are primarily composed of olivine, orthopyroxene, and clinopyroxene.

CG0944 – A coarse-grained leucotroctolite from the Kenemich massif of the Mealy Mountains Intrusive Suite located in the Eastern Grenville Province. It contains primarily plagioclase (~84%), orthopyroxene (~4%), olivine (~6%), and minor clinopyroxene (mineral volume % estimations based on CIPW normative mineral calculations from major oxide geochemical data). Olivine typically occurs as both a cumulus and intercumulus phase and is frequently fractured or altered to serpentine with clinopyroxene and orthopyroxene rims (Bybee, 2014) (sample provided by L.D. Ashwal).

San Carlos peridotite – Ultramafic inclusion of olivine-rich peridotite from Peridot Mesa on the San Carlos Indian Reservation, Arizona. It is primarily composed of olivine, orthopyroxene, clinopyroxene, and some interstitial spinel (mainly chromite-spinel) in order of their general modal proportions. It is very coarse-grained and has a xenomorphic-granular texture with some triple point junctions (Frey and Prinz, 1978).

## APPENDIX III: Data

We report data from analyses of three different types of lunar samples which include whole-rock samples, volcanic glass beads, and mineral separates obtained from NASA Johnson Space Center. The lunar samples selected were chosen for their high ranking on the pristinity index (Warren, 1993), and internal sample chips were requested to reduce the possibility of surficial contamination processes. The terrestrial samples chosen to represent bulk silicate Earth consisted primarily of mineral separates from basalt, gabbro, and peridotite samples and basaltic glasses obtained from various sources (see sample descriptions) as well as the UNM sample collection (Table 2).

**Table 2. Oxygen isotope data for lunar and terrestrial samples**

**Lunar Basalt**

| Sample | Type | n | $\delta^{17}O$ | 1σ | $\delta^{18}O$ | 1σ | $\delta'^{17}O$ | $\delta'^{18}O$ | $\Delta'^{17}O$ | 1σ |
|---|---|---|---|---|---|---|---|---|---|---|
| 10017.402 | Ilmenite Basalt (High K) | 2 | 2.878 | 0.027 | 5.564 | 0.055 | 2.874 | 5.549 | -0.056 | 0.001 |
| 10017.403 | Ilmenite Basalt (High K) | 2 | 2.989 | 0.051 | 5.776 | 0.095 | 2.985 | 5.759 | -0.056 | 0.001 |
| 10020.253 | Ilmenite Basalt (Low K) | 2 | 2.925 | 0.005 | 5.651 | <0.001 | 2.921 | 5.635 | -0.054 | 0.005 |
| 10044.653 | Ilmenite Basalt (Low K) | 4 | 3.092 | 0.070 | 5.961 | 0.138 | 3.088 | 5.943 | -0.050 | 0.008 |
| 12002.596 | Olivine Basalt | 1 | 2.792 | N/A | 5.379 | N/A | 2.788 | 5.365 | -0.045 | N/A |
| 12018.275 | Olivine Basalt | 4 | 2.880 | 0.049 | 5.542 | 0.097 | 2.876 | 5.526 | -0.042 | 0.004 |
| 12054.144 | Glass-coated Ilmenite Basalt | 4 | 2.981 | 0.035 | 5.757 | 0.063 | 2.976 | 5.740 | -0.055 | 0.004 |
| 12054.148 | Glass-coated Ilmenite Basalt | 4 | 3.023 | 0.070 | 5.832 | 0.136 | 3.018 | 5.815 | -0.052 | 0.005 |
| 12063.341 | Ilmenite Basalt | 2 | 2.910 | 0.068 | 5.587 | 0.131 | 2.905 | 5.571 | -0.036 | 0.001 |
| 14053.307 | Aluminous Mare Basalt | 6 | 3.005 | 0.091 | 5.806 | 0.174 | 3.000 | 5.790 | -0.057 | 0.009 |
| 15016.242 | Vesicular Olivine-normative Basalt | 2 | 2.875 | 0.041 | 5.528 | 0.090 | 2.871 | 5.512 | -0.039 | 0.006 |
| 15535.163 | Olivine-normative Basalt | 3 | 2.872 | 0.012 | 5.547 | 0.041 | 2.867 | 5.531 | -0.053 | 0.010 |
| 15556.256 | Vesicular Olivine-normative Basalt | 1 | 2.902 | N/A | 5.592 | N/A | 2.897 | 5.577 | -0.047 | N/A |
| 70215.390 | Mare Basalt | 4 | 2.872 | 0.125 | 5.545 | 0.234 | 2.867 | 5.529 | -0.052 | 0.005 |
| 70255.54 | Ilmenite Basalt | 4 | 2.881 | 0.022 | 5.560 | 0.044 | 2.877 | 5.545 | -0.051 | 0.005 |
| 71135.36 | Ilmenite Basalt | 4 | 2.895 | 0.015 | 5.585 | 0.028 | 2.891 | 5.569 | -0.050 | 0.008 |
| 71546.24 | Ilmenite Basalt | 4 | 2.937 | 0.063 | 5.663 | 0.113 | 2.933 | 5.647 | -0.049 | 0.004 |
| 74275.325 | Ilmenite Basalt | 2 | 2.765 | 0.088 | 5.338 | 0.160 | 2.761 | 5.324 | -0.050 | 0.004 |
| 75035.25 | Ilmenite Basalt | 2 | 3.044 | 0.037 | 5.865 | 0.072 | 3.039 | 5.848 | -0.049 | 0.001 |

**Table 2. Continued**

**Lunar Crust**

| Sample | Type | n | $\delta^{17}O$ | 1σ | $\delta^{18}O$ | 1σ | $\delta'^{17}O$ | $\delta'^{18}O$ | $\Delta'^{17}O$ | 1σ |
|---|---|---|---|---|---|---|---|---|---|---|
| 76335.74 | Cataclastic Magnesian Anorthosite | 2 | 3.139 | 0.051 | 6.069 | 0.084 | 3.134 | 6.051 | -0.061 | 0.009 |
| 78235.163 | Shocked Norite | 2 | 3.023 | 0.043 | 5.841 | 0.063 | 3.018 | 5.824 | -0.057 | 0.010 |

**Lunar Glass**

| Sample | Type | n | $\delta^{17}O$ | 1σ | $\delta^{18}O$ | 1σ | $\delta'^{17}O$ | $\delta'^{18}O$ | $\Delta'^{17}O$ | 1σ |
|---|---|---|---|---|---|---|---|---|---|---|
| 15426 | Green Glass | 2 | 2.952 | 0.025 | 5.655 | 0.049 | 2.947 | 5.639 | -0.030 | 0.001 |
| 74220 | Black Glass | 2 | 2.925 | 0.055 | 5.641 | 0.110 | 2.920 | 5.625 | -0.050 | 0.003 |

**Table 2. Continued**

**Lunar Separates**

| Sample | Type | n | $\delta^{17}O$ | 1σ | $\delta^{18}O$ | 1σ | $\delta'^{17}O$ | $\delta'^{18}O$ | $\Delta'^{17}O$ | 1σ |
|---|---|---|---|---|---|---|---|---|---|---|
| 10017 (Ilmenite) | Ilmenite Basalt (High K) | 3 | 2.471 | 0.100 | 4.773 | 0.190 | 2.468 | 4.762 | -0.047 | 0.003 |
| 15535 (Pyroxene) | Olivine-normative Basalt | 4 | 2.786 | 0.018 | 5.351 | 0.043 | 2.782 | 5.337 | -0.036 | 0.003 |
| 15535 (Plagioclase) | Olivine-normative Basalt | 3 | 2.962 | 0.065 | 5.726 | 0.122 | 2.957 | 5.710 | -0.058 | 0.006 |
| 15556 (Pyroxene) | Vesicular Olivine-normative Basalt | 2 | 2.717 | 0.028 | 5.214 | 0.047 | 2.713 | 5.200 | -0.033 | 0.003 |
| 15556 (Plagioclase) | Vesicular Olivine-normative Basalt | 3 | 2.905 | 0.070 | 5.616 | 0.135 | 2.901 | 5.601 | -0.056 | 0.001 |
| 60016 (Pyroxene) | Ancient Regolith Breccia | 2 | 2.691 | 0.003 | 5.229 | 0.003 | 2.687 | 5.215 | -0.067 | 0.001 |
| 62237 (Olivine) | Troctolitic Anorthosite | 2 | 2.468 | 0.050 | 4.817 | 0.090 | 2.465 | 4.805 | -0.072 | 0.003 |
| 60016 (Plagioclase) | Ancient Regolith Breccia | 2 | 2.883 | 0.076 | 5.583 | 0.158 | 2.878 | 5.568 | -0.061 | 0.007 |
| 62237 (Plagioclase) | Troctolitic Anorthosite | 2 | 2.932 | 0.053 | 5.685 | 0.095 | 2.928 | 5.669 | -0.065 | 0.003 |
| 71135 (Ilmenite) | Ilmenite Basalt | 2 | 2.525 | 0.078 | 4.876 | 0.150 | 2.522 | 4.864 | -0.046 | 0.001 |
| 75035 (Pyroxene) | Ilmenite Basalt | 2 | 2.932 | 0.013 | 5.671 | 0.041 | 2.928 | 5.655 | -0.058 | 0.008 |
| 75035 (Plagioclase) | Ilmenite Basalt | 3 | 3.255 | 0.076 | 6.274 | 0.132 | 3.250 | 6.254 | -0.052 | 0.007 |
| 75035 (Ilmenite) | Ilmenite Basalt | 3 | 2.541 | 0.048 | 4.917 | 0.096 | 2.537 | 4.905 | -0.053 | 0.002 |
| 76535 (Olivine) | Troctolite | 1 | 2.757 | N/A | 5.303 | N/A | 2.753 | 5.289 | -0.040 | N/A |
| 76535 (Plagioclase) | Troctolite | 1 | 2.867 | N/A | 5.526 | N/A | 2.862 | 5.511 | -0.047 | N/A |
| 77215 (Pyroxene) | Cataclastic Norite | 2 | 2.726 | 0.123 | 5.245 | 0.248 | 2.722 | 5.231 | -0.040 | 0.008 |
| 77215 (Plagioclase) | Cataclastic Norite | 2 | 2.857 | 0.037 | 5.509 | 0.069 | 2.853 | 5.494 | -0.049 | 0.001 |
| 78238 (Pyroxene) | Shocked Norite | 2 | 2.685 | 0.074 | 5.197 | 0.131 | 2.681 | 5.183 | -0.056 | 0.005 |
| 78238 (Plagioclase) | Shocked Norite | 2 | 2.832 | 0.086 | 5.460 | 0.158 | 2.828 | 5.446 | -0.047 | 0.003 |

**Table 2. Continued**

**Terrestrial Samples (Bulk Earth)**

| Sample | Type | n | $\delta^{17}O$ | 1σ | $\delta^{18}O$ | 1σ | $\delta'^{17}O$ | $\delta'^{18}O$ | $\Delta'^{17}O$ | 1σ |
|---|---|---|---|---|---|---|---|---|---|---|
| KE58-2842F | Hawaiian Basaltic Glass | 4 | 2.639 | 0.126 | 5.106 | 0.239 | 2.635 | 5.093 | -0.054 | 0.004 |
| ALV2772-1 | MORB Glass | 2 | 2.721 | 0.016 | 5.256 | 0.025 | 2.717 | 5.242 | -0.051 | 0.003 |
| ALV2746-12 | MORB Glass | 2 | 2.827 | 0.059 | 5.465 | 0.113 | 2.823 | 5.450 | -0.055 | 0.000 |
| MAQ25637 | Macquarie Isl. Basaltic Glass | 1 | 2.901 | N/A | 5.610 | N/A | 2.896 | 5.595 | -0.058 | N/A |
| MAQ82 | Macquarie Isl. Basaltic Glass | 1 | 2.686 | N/A | 5.202 | N/A | 2.682 | 5.188 | -0.057 | N/A |
| MAQ47979 | Macquarie Isl. Basaltic Glass | 2 | 2.851 | 0.053 | 5.515 | 0.102 | 2.847 | 5.500 | -0.057 | 0.000 |
| DUNA | Addie Quarry Dunite | 2 | 2.963 | 0.036 | 5.720 | 0.068 | 2.959 | 5.704 | -0.053 | 0.001 |

**Table 2. Continued**

**Terrestrial Mineral Separates (Bulk Earth)**

| Sample | Type | n | $\delta^{17}O$ | 1σ | $\delta^{18}O$ | 1σ | $\delta'^{17}O$ | $\delta'^{18}O$ | $\Delta'^{17}O$ | 1σ |
|---|---|---|---|---|---|---|---|---|---|---|
| TPS-03 (Orthopyroxene) | Antarctic Basalt Sill | 3 | 3.094 | 0.062 | 5.957 | 0.124 | 3.089 | 5.939 | -0.047 | 0.004 |
| TPS-02 (Orthopyroxene) | Antarctic Basalt Sill | 2 | 3.169 | 0.009 | 6.108 | 0.018 | 3.164 | 6.089 | -0.052 | 0.001 |
| MC-OL (Olivine) | Mesa Chivato Basalt | 1 | 2.629 | N/A | 5.084 | N/A | 2.625 | 5.071 | -0.052 | N/A |
| MC-PX (Pyroxene) | Mesa Chivato Basalt | 2 | 2.551 | 0.168 | 4.939 | 0.327 | 2.548 | 4.926 | -0.053 | 0.004 |
| ST15-01A (Olivine) | Kimberley Granular Peridotite | 2 | 2.593 | 0.003 | 5.006 | 0.008 | 2.590 | 4.993 | -0.047 | 0.001 |
| ST15-01A (Orthopyroxene) | Kimberley Granular Peridotite | 2 | 2.722 | 0.069 | 5.271 | 0.137 | 2.718 | 5.257 | -0.057 | 0.003 |
| GAB-PX (Pyroxene) | Duluth Gabbro | 2 | 2.600 | 0.034 | 5.034 | 0.048 | 2.597 | 5.021 | -0.055 | 0.008 |
| FINPP-OL (Olivine) | Finero Peridotite | 2 | 2.760 | 0.009 | 5.330 | 0.014 | 2.756 | 5.316 | -0.050 | 0.002 |
| FINPP-OPX (Orthopyroxne) | Finero Peridotite | 2 | 3.120 | 0.018 | 6.026 | 0.029 | 3.115 | 6.008 | -0.057 | 0.003 |
| ANT-OL (Olivine) | Antarctic Peridotite | 1 | 2.758 | N/A | 5.317 | N/A | 2.754 | 5.302 | -0.046 | N/A |
| ANT-PX (Pyroxene) | Antarctic Peridotite | 1 | 3.056 | N/A | 5.887 | N/A | 3.051 | 5.870 | -0.049 | N/A |
| FSM-OL (Olivine) | Ferrel Seamount Peridotite | 2 | 2.800 | 0.018 | 5.401 | 0.041 | 2.796 | 5.386 | -0.048 | 0.003 |
| FSM-OPX (Orthopyroxene) | Ferrel Seamount Peridotite | 2 | 3.076 | 0.059 | 5.926 | 0.126 | 3.071 | 5.908 | -0.048 | 0.007 |
| FSM-CPX (Clinopyroxene) | Ferrel Seamount Peridotite | 2 | 2.629 | 0.111 | 5.082 | 0.200 | 2.625 | 5.069 | -0.051 | 0.005 |
| SCO (Olivine) | San Carlos Peridotite | 44 | 2.706 | 0.074 | 5.226 | 0.138 | 2.702 | 5.213 | -0.050 | 0.004 |

**Table 2. Continued**

**Terrestrial Mineral Separates (Non-Bulk Earth)**

| Sample | Type | n | $\delta^{17}O$ | 1σ | $\delta^{18}O$ | 1σ | $\delta'^{17}O$ | $\delta'^{18}O$ | $\Delta'^{17}O$ | 1σ |
|---|---|---|---|---|---|---|---|---|---|---|
| TPS-03 (Plagioclase A) | Antarctic Basalt | 3 | 3.266 | 0.085 | 6.309 | 0.158 | 3.260 | 6.289 | -0.060 | 0.003 |
| TPS-03 (Plagioclase B) | Antarctic Basalt | 3 | 3.219 | 0.118 | 6.219 | 0.220 | 3.214 | 6.200 | -0.060 | 0.002 |
| MC-PL (Plagioclase) | Mesa Chivato Basalt | 2 | 3.554 | 0.139 | 6.835 | 0.275 | 3.548 | 6.812 | -0.049 | 0.005 |
| GAB-PL (Plagioclase) | Duluth Gabbro | 2 | 3.261 | 0.080 | 6.304 | 0.138 | 3.256 | 6.284 | -0.062 | 0.007 |
| MT-PX (Pyroxene) | Mt. Taylor Basalt | 2 | 2.506 | 0.041 | 4.822 | 0.083 | 2.503 | 4.810 | -0.037 | 0.002 |
| MT-PL (Plagioclase) | Mt. Taylor Basalt | 3 | 2.969 | 0.069 | 5.705 | 0.131 | 2.964 | 5.689 | -0.039 | 0.006 |
| CG0944 (Bronzite) | Labrador Anorthosite | 4 | 3.616 | 0.170 | 6.978 | 0.326 | 3.610 | 6.954 | -0.062 | 0.011 |
| CG0944 (Plagioclase) | Labrador Anorthosite | 4 | 3.950 | 0.183 | 7.611 | 0.343 | 3.943 | 7.582 | -0.061 | 0.006 |

## APPENDIX IV: Triple Oxygen Isotope Systematics

In order to understand some of the concepts within this paper, it is necessary to briefly introduce some foundational information regarding the triple oxygen isotope system and its use. Early on, in the formative days of stable isotope research, it was recognized that measuring the rare $^{17}O$ of a substance provided little to no additional information over determining the $\delta^{18}O$ value (Bigeleisen, 1952; Craig, 1957). This is because they identified a relationship in that $\delta^{17}O$ was found to be approximately one half of $\delta^{18}O$, where $\delta^{x}O$ is given by:

$$\delta^{x}O = \left(\frac{R_{sample}}{R_{standard}} - 1\right) \times 1000 \qquad \text{(eq. 1)}$$

where R is the $^{18}O/^{16}O$ or $^{17}O/^{16}O$ ratio, depending on *x*. However, small, mass dependent deviations in fractionation from this near linear relationship exist. When dealing with the high precision analyses required for working with the triple oxygen isotope system, it has been suggested to use a linearized form of delta notation (Young et al., 2002; Miller, 2002; Luz and Barkan, 2005), which is denoted by ($\delta'$) where:

$$\delta' = 1000\, ln\left(\frac{\delta}{1000} + 1\right) \qquad \text{(eq. 2)}$$

For the triple oxygen isotope system, mass dependent fractionation between two phases A and B, in thermodynamic equilibrium is given by the equation:

$$\alpha^{17}O_{A-B} = (\alpha^{18}O_{A-B})^{\theta} \qquad \text{(eq. 3)}$$

(Young et al., 2002; Pack and Herwartz, 2014; Sharp et al., 2016). In linearized form, this equation is given as:

$$ln\alpha^{17}O_{A-B} = \theta(ln\alpha^{18}O_{A-B}) \quad \text{(eq. 4)}$$

(Sharp et al., 2016), where θ is the triple isotope fractionation exponent, which can be further defined by the equation:

$$\theta_{A-B} = \frac{\delta'^{17}O_A - \delta'^{17}O_B}{\delta'^{18}O_A - \delta'^{18}O_B} \quad \text{(eq. 5)}$$

(Sharp et al., 2016). The terrestrial fractionation line (TFL) is the line in $\delta^{17}O$-$\delta^{18}O$ space along which all terrestrial values plot. The general equation for the linearized form of the TFL is given as:

$$\delta'^{17}O = \lambda \times \delta'^{18}O + \gamma \quad \text{(eq. 6)}$$

where λ is defined as the empirically derived slope of the best fit line for this data and γ is the y-intercept (Sharp et al., 2016). The γ term is normally taken as zero. Small departures from the TFL, which are the main focus of this paper, are best illustrated using the $\Delta'^{17}O$ notation where:

$$\Delta'^{17}O = \delta'^{17}O_{measured} - \lambda \times \delta'^{18}O \quad \text{(eq. 7)}$$

From Equation 7 we can see that the $\Delta'^{17}O$ is defined as the difference between the actual $\delta'^{17}O_{measured}$ value of the substance and the $\delta'^{17}O$ calculated from Equation 6 using a defined $\lambda$ value. Throughout this work we use a $\lambda$ value of 0.528 for reasons explained in Sharp *et al.* (2018). Other researchers have used alternative values for $\lambda$ (e.g. Herwartz et al., 2014; Greenwood et al., 2018), however it is important to note that the choice of a $\lambda$ value is arbitrary since it only serves as a numerical placeholder when making the $\Delta'^{17}O$ calculation. This does mean that $\Delta'^{17}O$ values will vary between studies using different $\lambda$ values, which is why when comparing $\Delta'^{17}O$ values in this work to others, it is important to recalculate the $\Delta'^{17}O$ value using the appropriate $\lambda$.

## APPENDIX V: Comparisons to Previous Work

**Herwartz *et al*. (2014):** In order to compare these data with previous data, the results for San Carlos olivine must be used to normalize all other data sets to our reference frame. If, as in this case the previous researchers used a different λ value, $\Delta'^{17}O$ is recalculated with a λ value of 0.528 and adoption of the $\delta'^{17}O$ and $\delta'^{18}O$ value of San Carlos olivine of 2.702 and 5.213 ‰, respectively (Table 1). This normalization to SC olivine and recalculation of $\Delta'^{17}O$ is necessary to have a valid comparison between studies.

Two of the three lunar samples measured by Herwartz *et al.* (2014) were also measured in this study, samples 10017 and 12018. Comparison of the data obtained for sample 10017 reveals that the $\delta'^{18}O$ values are similar within the margins of error, but the $\Delta'^{17}O$ values differ drastically, with their results measuring +0.017 ‰ heavier than our value of -0.056‰. The comparative $\Delta'^{17}O$ values for sample 12018 differed by significantly less and agreed within the range of 1σ standard deviation, however they still measured slightly heavier than our data.

**Young *et al.* (2016):** These data were also normalized to San Carlos olivine and recalculated for λ = 0.528 using the same process described for Herwartz *et al.* (2014). Figure 4 shows the data from Young *et al.* (2016) plotted in a similar fashion to our Figure 2 from the paper. Comparing these plots, we can see that their crustal samples display similar light $\Delta'^{17}O$ values to those measured in this study. However, the high- and low-Ti basalts do not display the same difference seen in our results; though it should be noted that their results for high- and low-Ti basalts vary across much larger ranges than what is seen in this study. Sample 12018 was measured in both studies and were

found to be nearly identical. The lack of distinction between the high- and low-Ti basalts in Young *et al.* (2016) might be due to the selection of samples measured. Only four low-Ti basalts and two high-Ti basalts were measured in their lunar sample suite, which may not be enough to flesh out the distinction since anomalous samples can have a larger effect on the $\Delta'^{17}O$ averages for each separate lithology.

**Greenwood *et al*. (2018):** These data were normalized to San Carlos olivine and recalculated for $\lambda = 0.528$ using the same method described above. Figure 5 shows these data plotted in a similar fashion to our Figure 2 from the paper. When separated into the different lithologies, the data from Greenwood *et al.* (2018) shows the most similarities to our data from this study. A similar trend of decreasing $\Delta'^{17}O$ values can be seen with the increasing degree of contamination from the light vapor incorporation. The difference between the means for their high- and low-Ti basalts is about half the size of the difference seen in our data set, however this could once again come down to sample selection. It should be noted that based on samples that were measured in both studies (10020, 10044, 14053, 78235) our $\Delta'^{17}O$ values tended to measure lighter than those reported in Greenwood *et al.* (2018), but the values still fall within 1σ standard deviation of each other.

**Hallis *et al.* (2010), Spicuzza *et al.* (2007), Wiechert *et al.* (2001):** Since San Carlos olivine was not measured in these studies and UWG-2 was not measured in ours, the measurements of UWG-2 and SC olivine from Young *et al.* (2016) was used as an intermediate step in the normalization of these data. First, the results from Hallis *et al.* (2010), Spicuzza *et al*. (2007), and Wiechert *et al.* (2001) were all normalized to the UWG-2 garnet measurements from Young *et al.* (2016) These values were then

subsequently normalized to our frame of reference using the SC olivine data from Young *et al.* (2016), and the $\Delta'^{17}O$ was recalculated using a $\lambda$ value of 0.528.

Plotting these data in Figures 6, 7, and 8 displays the large amount of spread in $\Delta'^{17}O$ values that was present in the studies prior to Herwartz *et al.* (2014), and these large ranges for both high- and low-Ti basalts masks any discernable difference between the two. Due to the larger errors on the $\Delta'^{17}O$ values from these measurements, its unsurprising that the small lithology-based variation we've identified in this paper was previously unrecognized. While no clear difference can be discerned between the high- and low-Ti basalts from these studies, Wiechert *et al.* (2001) did measure a distinct difference between the mare basalts and the lunar crustal samples, which had considerably lower $\Delta'^{17}O$ values that were in the range of what would be expected given our data.

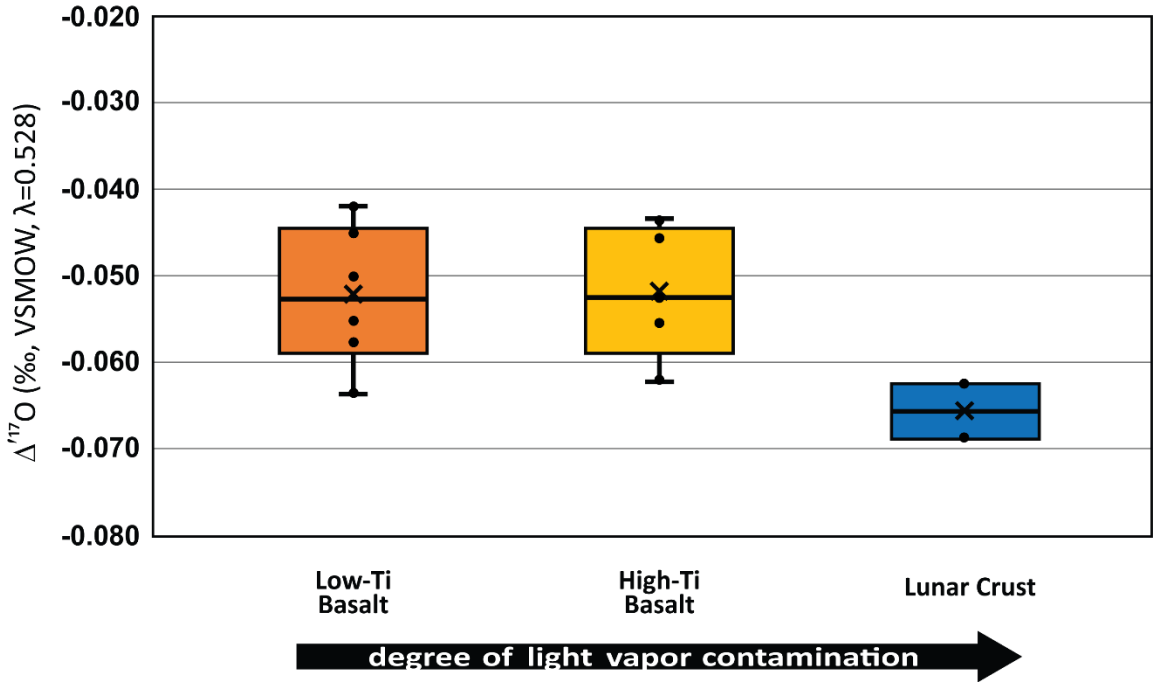


**Fig. 4. Young *et al*. (2016): Box and whisker plot showing the $\Delta'^{17}O$ values for the different lunar lithologies.** The bar within the boxes indicate the median value, and the X denotes the mean value.

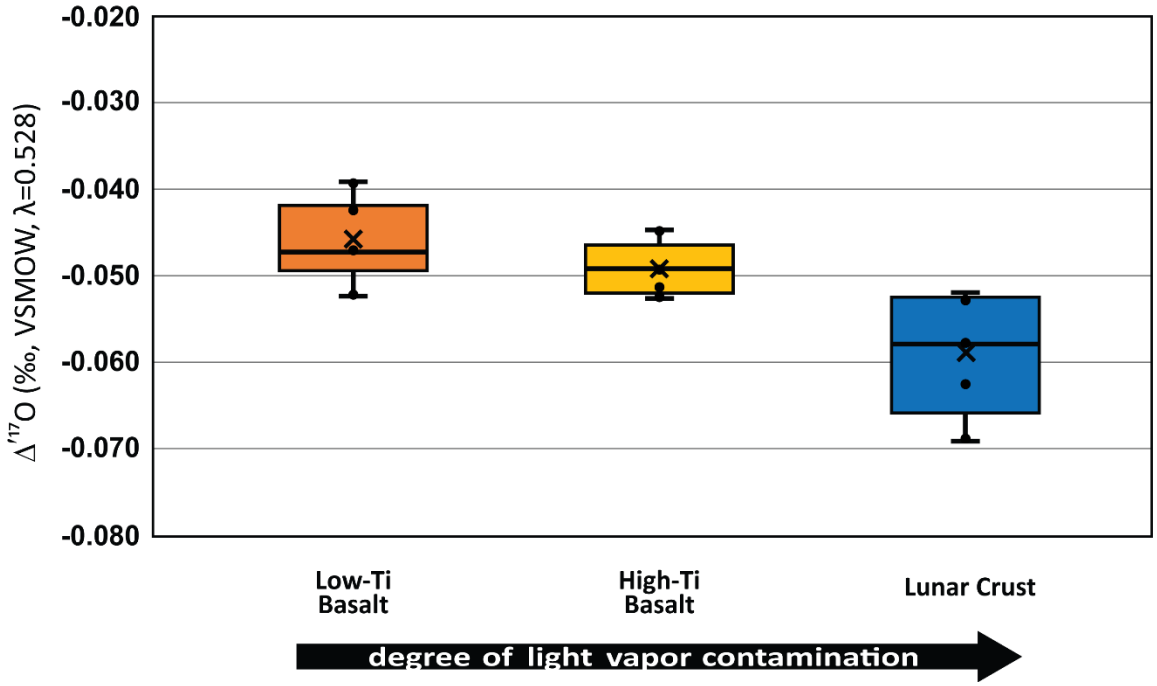


**Fig. 5. Greenwood *et al*. (2018): Box and whisker plot showing the $\Delta'^{17}O$ values for the different lunar lithologies.** The bar within the boxes indicate the median value, and the X denotes the mean value.

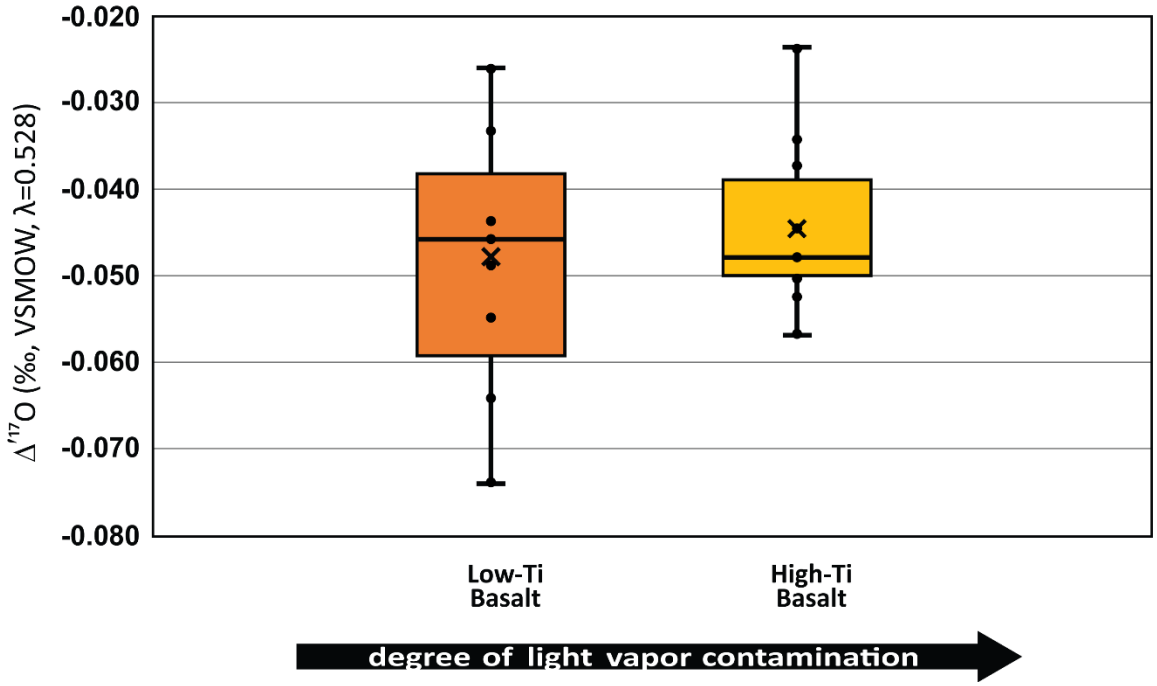


**Fig. 6. Hallis *et al*. (2010): Box and whisker plot showing the $\Delta'^{17}O$ values for the different lunar lithologies.** The bar within the boxes indicate the median value, and the X denotes the mean value.

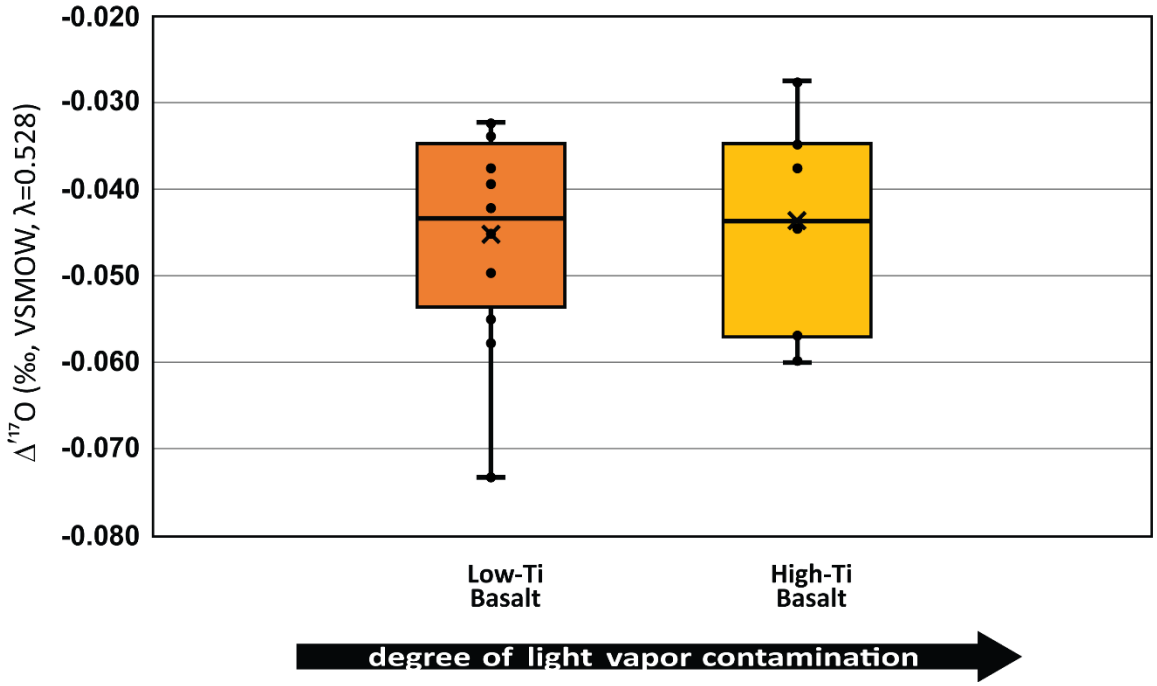


**Fig. 7. Spicuzza *et al*. (2007): Box and whisker plot showing the $\Delta'^{17}O$ values for the different lunar lithologies.** The bar within the boxes indicate the median value, and the X denotes the mean value.

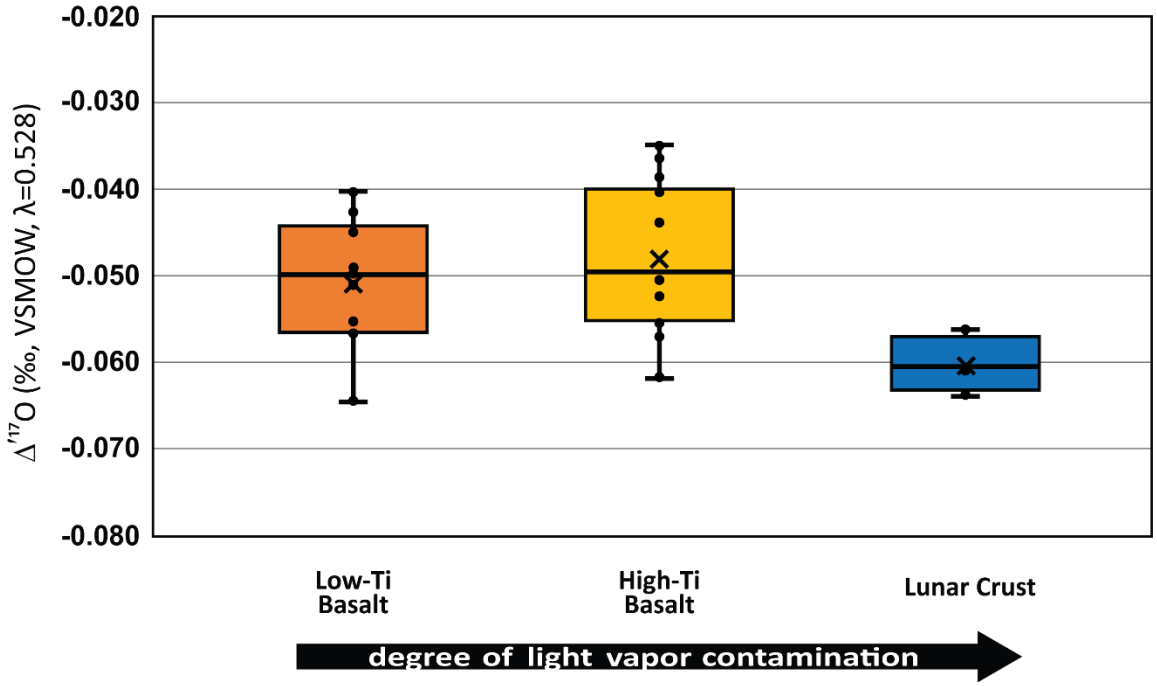


**Fig. 8. Wiechert *et al.* (2001): Box and whisker plot showing the $\Delta'^{17}O$ values for the different lunar lithologies.** The bar within the boxes indicate the median value, and the X denotes the mean value.

## APPENDIX VI: Mineral-specific isotope effects

It has been noted previously that lunar samples dominated by plagioclase (i.e. FANs and anorthositic crustal rocks) systematically measure lower in $\Delta'^{17}O$ than other samples measured (Young et al., 2016; Kohl et al., 2017; Cano et al., 2017). It was suggested that this could be attributed to an unknown mineral-specific chemical effect, specific to the tectosilicate lattice structure of plagioclase, that could favorably partition $O^{17}$ into one mineral over the other (Kohl et al., 2017). The implications of this effect would call into question the fundamental principles of how fractionation factors vary with equilibration temperature.

In order to test this possibility, we measured the oxygen isotope compositions of mineral separates from terrestrial basalts and gabbros (Fig. 9B). All samples except one have high θ values (~0.522 to ~0.530) consistent with a general increase in θ with increasing temperature (Pack and Herwartz, 2014; Sharp et al., 2018). One sample (TPS-03) from a basaltic sill in Antarctica (Wilhelm and Wörner, 1996) has $\theta_{plag\text{-}pyroxene}$ values of 0.478 to 0.488 (Fig. 9B), which we attribute to hydrothermal alteration of the intrusive unit, a common feature in mafic intrusives (Norton and Taylor, 1979).

The crustal lunar samples (Fig. 9A) showed the largest range in θ values (~0.492 to ~0.560), the extremes of which are far outside the ranges expected for high temperature equilibration. These θ values, along with the large variation in $\Delta'^{17}O$ for crustal samples suggests that the pyroxene and plagioclase in these rocks likely formed out of equilibrium conditions with each other. Furthermore, some mineral phases may have incorporated different amounts of the light vapor component depending on when they crystalized and when the contamination took place. Since nearly all of our crustal

samples are from the Mg suite of lunar rocks, which are thought to have intruded the preexisting ferroan anorthositic crust (Shearer et al., 2006), it is plausible that the mineral phases exhibiting higher $\Delta'^{17}O$ values crystallized prior to the incorporation of lighter vapor contaminated material, lending to the large variation seen in these samples.

The θ value for one high-Ti basalt (75035) is consistent with the expected high temperature equilibration (Fig. 9A). Two low-Ti basalts (15535 and 15556) both have anomalous θ values of 0.470 (Fig. 9A). In those samples, the $\Delta'^{17}O$ value of the plagioclase is significantly lower than that of the pyroxene, matching the terrestrial basaltic sill (TPS-03). We suggest that the low $\Delta'^{17}O$ value is the result of the plagioclase crystals forming out of equilibrium with the pyroxene, and possibly incorporating a larger fraction of the light lunar vapor component.

It appeared that the relationship between higher $TiO_2$ content and lower $\Delta'^{17}O$ values could be related to a similar mineral-specific process possibly involving ilmenite. If ilmenite had an exceptionally low $\Delta'^{17}O$ value, then their high abundance in the high-Ti basalts could be affecting the bulk sample $\Delta'^{17}O$ measurements. Analyses of pyroxene, plagioclase, and ilmenite separates from the high-Ti basalts produced θ values consistent with predicted high-temperature equilibrium fractionation and the $\Delta'^{17}O$ values for ilmenite are nearly identical the whole rock analysis (Table 2). Furthermore, the two glass samples (15426 and 74220) fit in with the trend illustrated in Fig. 2 and are not affected by any crystallographic effects. We therefore ruled out the possibility that the proposed “crystal-chemical” effect or any other mineral-specific processes were contributing to the light $\Delta'^{17}O$ values obtained from the whole rock analyses of the high-

Ti basalts. Instead, the $\Delta'^{17}O$-$TiO_2$ relationship had to be linked to the petrogenic sources for these basalts.

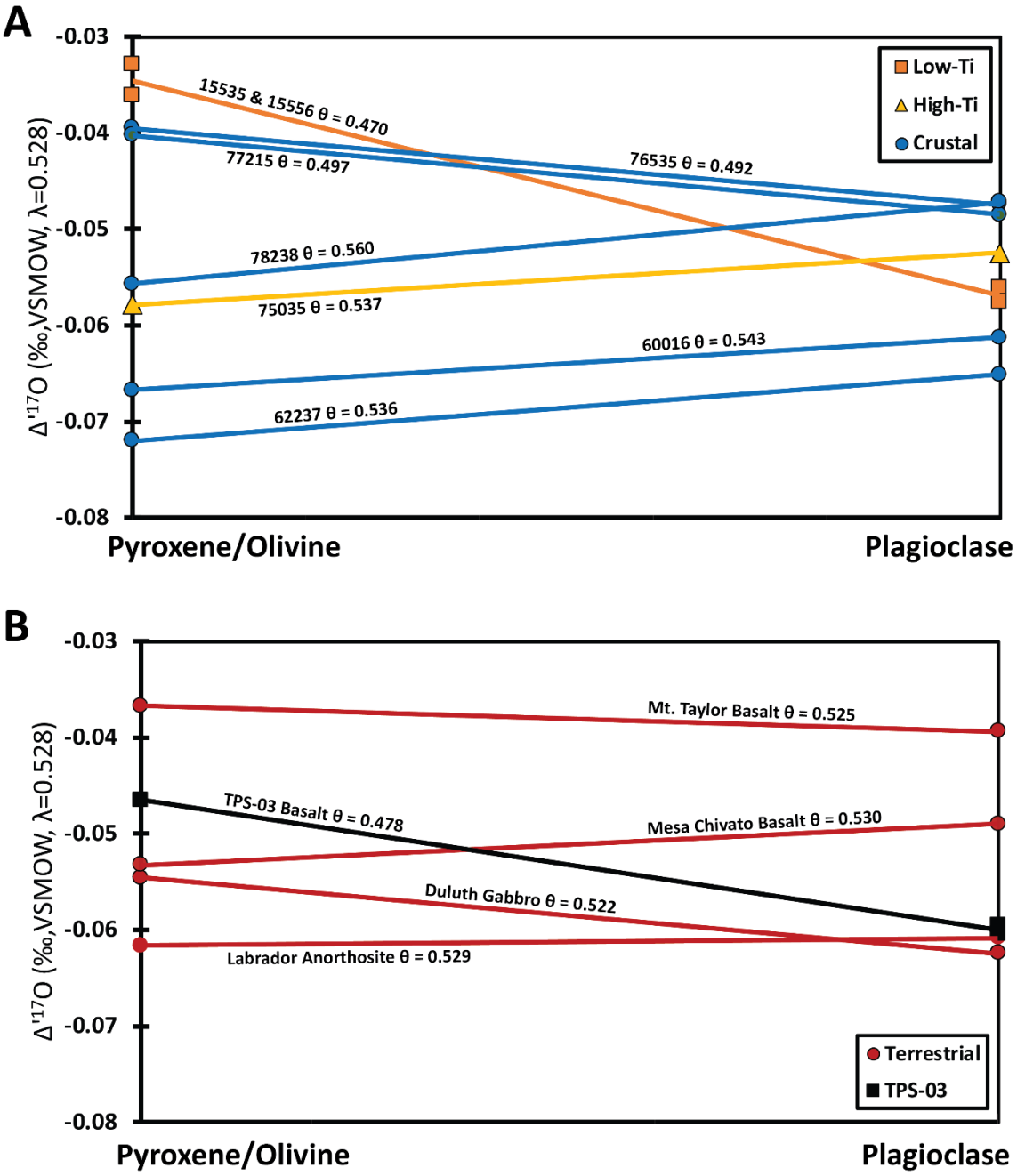


**Fig. 9. Plot showing the plagioclase – pyroxene/olivine mineral pair θ values for (A) lunar and (B) terrestrial samples.** $\Delta'^{17}O$ values for pyroxene and olivine separates are on the right side of the plot, and values for plagioclase separates are on the left side of the plot. Theta θ values are indicated along the line connecting the mineral pair. **(A)** The mineral separate data are plotted for the lunar samples including two low-Ti basalts, a high-Ti basalt, and crustal rocks including one FAN sample (62237). A single line represents samples 15535 and 15556 due to the slopes for their measured pairs being nearly identical. **(B)** The mineral separate data are plotted for the terrestrial samples including three basalts, a gabbro, and an anorthosite. The TPS-03 basalt is the only terrestrial sample measured that has a θ value similar to the low-Ti lunar basalts.

## APPENDIX VII: Anomalous Samples

Several samples that were measured for this study were omitted from the plotted results because they were anomalous with respect to $\Delta'^{17}O$, and it was unclear whether they should be included with their respective lithologies. Sample 12054, a glass-coated ilmenite basalt of which we measured chips 12054.144 and 12054.148, was not included in plotting Figures 2 and 3 from the paper. These were excluded due to the risk of possible contamination from the glass coating material. Even though internal samples were originally requested, it is unclear from where in the sample the chip we received originated. Sample 14053 was also not included in Figures 2 and 3 from the paper due to its classification as an aluminous mare basalt (Irving, 1975). While the characteristics of the aluminous mare basalts share some affinity with other mare basalts, researchers have suggested a source region between the crust and mantle (Reid and Jakes, 1974) or that they represent a mare basalt "contaminated at depth" with KREEP basalt (Schonfeld and Meyer, 1972). The final lunar sample that was excluded from Figure 2 and 3 was 15535, which is an olivine-normative basalt that returned an abnormally low $\Delta'^{17}O$ value in comparison to other olivine basalts. The standard deviation for all replicated runs of this standard is abnormally high when compared to the other basalt samples. This likely indicates that the composition of the sample is fairly heterogeneous and $\Delta'^{17}O$ values could vary significantly depending on the relative portions of olivine, pyroxene, and plagioclase in portion measured. Mineral separate data from this sample indicated that the plagioclase (-0.056‰) had a lower $\Delta'^{17}O$ value than the coexisting pyroxene (-0.036‰). Therefore, if the portion of sample material measured had an elevated amount of plagioclase, the result could be skewed toward a lower $\Delta'^{17}O$ value. The low $\Delta'^{17}O$ value

of the plagioclase relative to the olivine suggests that the former may have had some addition from the low $\Delta'^{17}O$ vapor component that may have occurred post olivine formation.

## APPENDIX VIII: Statistical Analyses

We performed several student *t* tests on the high- and low-Ti basalt groups as well as the terrestrial samples to determine if there was a statistically significant difference for $\Delta'^{17}O$ between these groups of data, the results of which are in Tables 3-8.

**Table 3. Results of student *t*-test assuming unequal variances for the low- and high-Ti groups**

| | *Low-Ti* | *High-Ti* |
|---|---|---|
| Mean | -0.040042 | -0.051529 |
| Variance | 0.0000391 | 0.0000073 |
| Observations | 6 | 11 |
| Hypothesized Mean Difference | 0 | |
| df | 6 | |
| t Stat | 4.288274 | |
| P(T<=t) one-tail | 0.002579 | |
| t Critical one-tail | 1.94318 | |
| P(T<=t) two-tail | 0.005159 | |
| t Critical two-tail | 2.446912 | |

In this test (Table 3) the two-tail P value is well below the 0.05 alpha value used for the test, suggesting that there is a clear significant difference between the means of the groups. Additionally, the t-value (t stat) is considerably larger than the two-tail t-critical value, further indicating that the data for the low- and high-Ti basalts are significantly different from each other. It should be noted that for this test the low-Ti group includes the whole-rock low-Ti basalt data as well as the very-low-Ti green glass data while excluding the anomalous samples described in the previous section. The high-Ti group includes the whole-rock high-Ti basalt data as well as the high-Ti black glass data.

**Table 4. Results of student *t*-test assuming unequal variances for the low- and high-Ti groups including mineral separates.**

| | *Low-Ti* | *High-Ti* |
|---|---|---|
| Mean | -0.03866 | -0.051292 |
| Variance | 0.0000352 | 0.0000094 |
| Observations | 8 | 16 |
| Hypothesized Mean Difference | 0 | |
| df | 9 | |
| t Stat | 5.6580871 | |
| P(T<=t) one-tail | 0.0001552 | |
| t Critical one-tail | 1.8331129 | |
| P(T<=t) two-tail | 0.0003104 | |
| t Critical two-tail | 2.2621572 | |

In this test (Table 4) the two-tail P value is well below the 0.05 alpha value used for the test, suggesting that there is a clear significant difference between the means of the groups. Additionally, the t-value (t stat) is considerably larger than the two-tail t-critical value, and it is also larger than the t-value from the previous test (Table 3). This is further indication that the data for the low- and high-Ti basalts are significantly different from each other, and the addition of the mineral separates has increased the degree to which they are different. This version of the test includes all data from the previous test (Table 3) with the addition of pyroxene mineral separate values from samples 15535 and 15556 to the low-Ti group. The plagioclase separate data was not included for 15535 and 15556 due to the plagioclase appearing to be out of equilibrium, as noted in the mineral specific isotope effects section above. Furthermore, the high-Ti group includes the addition of pyroxene, plagioclase, and ilmenite separate data from sample 75035 and ilmenite separate data from samples 71135 and 10017.

**Table 5. Results of student *t*-test assuming unequal variances for the low- and high-Ti groups including mineral separates and anomalous samples.**

| | *Low-Ti* | *High-Ti* |
|---|---|---|
| Mean | -0.0426834 | -0.0512915 |
| Variance | 0.0000724 | 0.0000094 |
| Observations | 11 | 16 |
| Hypothesized Mean Difference | 0 | |
| df | 12 | |
| t Stat | 3.2157021 | |
| P(T<=t) one-tail | 0.0037067 | |
| t Critical one-tail | 1.7822876 | |
| P(T<=t) two-tail | 0.0074134 | |
| t Critical two-tail | 2.1788128 | |

In this test (Table 5) the two-tail P value is well below the 0.05 alpha value used for the test, suggesting that, despite the inclusion of the anomalous samples measured, there is still a significant difference between the means of the groups. The t-value (t stat) is not as large as in previous tests (Tables 3 and 4), indicating a smaller difference between the two groups, however it is still larger than the two-tail t-critical value. This means that a statistically significant difference between data for the low- and high-Ti basalt groups still exists. Please note that this version of the test includes all data from the previous test (Table 4) with the addition of the anomalous values for samples 12054.144,148 and 15535 included in the low-Ti data group. Sample 14053 was still omitted from this test due to the possibility of its petrogenesis being unrelated to the other mare basalts.

**Table 6. Results of student *t*-test assuming unequal variances for the low-Ti basalts and bulk silicate Earth**

| | *Low-Ti* | *Earth* |
|---|---|---|
| Mean | -0.040042 | -0.051549 |
| Variance | 0.0000391 | 0.0000136 |
| Observations | 6 | 23 |
| Hypothesized Mean Difference | 0 | |
| df | 6 | |
| t Stat | 4.316984 | |
| P(T<=t) one-tail | 0.0025 | |
| t Critical one-tail | 1.94318 | |
| P(T<=t) two-tail | 0.004999 | |
| t Critical two-tail | 2.446912 | |

In this test (Table 6) the two-tail P value is well below the 0.05 alpha value used for the test, suggesting that there is a clear significant difference between the means of the groups. Additionally, the t-value (t stat) is considerably larger than the two-tail t-critical value, further indicating that the data for the low-Ti basalts and bulk silicate Earth are significantly different from each other. It should be noted that for this test the low-Ti group includes the whole-rock low-Ti basalt data as well as the very-low-Ti green glass data while excluding the anomalous samples described in the previous section. The bulk silicate Earth group includes all values obtained for the terrestrial sample suite.

**Table 7. Results of student *t*-test assuming unequal variances for the low-Ti basalts and bulk silicate Earth including low-Ti mineral separates.**

| | *Low-Ti* | *Earth* |
|---|---|---|
| Mean | -0.03866 | -0.051549 |
| Variance | 0.0000352 | 0.0000136 |
| Observations | 8 | 23 |
| Hypothesized Mean Difference | 0 | |
| df | 9 | |
| t Stat | 5.772153 | |
| P(T<=t) one-tail | 0.000134 | |
| t Critical one-tail | 1.833113 | |
| P(T<=t) two-tail | 0.000269 | |
| t Critical two-tail | 2.262157 | |

In this test (Table 7) the two-tail P value is well below the 0.05 alpha value used for the test, suggesting that there is a clear significant difference between the means of the groups. Additionally, the t-value (t stat) is considerably larger than the two-tail t-critical value, and it is also larger than the t-value from the previous test (Table 6). This is further indication that the data for the low-Ti and bulk silicate Earth are significantly different from each other, and the addition of the mineral separates has increased the degree to which they are different. This version of the test includes all data from the previous test (Table 6) with the addition of pyroxene mineral separate values from samples 15535 and 15556 to the low-Ti group. The bulk silicate Earth group remained unchanged.

**Table 8. Results of student *t*-test assuming unequal variances for the low-Ti basalts and bulk silicate Earth including low-Ti mineral separates and anomalous samples.**

| | *Low-Ti* | *Earth* |
|---|---|---|
| Mean | -0.0426834 | -0.0515493 |
| Variance | 0.0000724 | 0.0000136 |
| Observations | 11 | 23 |
| Hypothesized Mean Difference | 0 | |
| df | 12 | |
| t Stat | 3.3114434 | |
| P(T<=t) one-tail | 0.0031039 | |
| t Critical one-tail | 1.7822876 | |
| P(T<=t) two-tail | 0.0062078 | |
| t Critical two-tail | 2.1788128 | |

In this test (Table 8) the two-tail P value is well below the 0.05 alpha value used for the test, suggesting that, despite the inclusion of the anomalous samples measured, there is still a significant difference between the means of the groups. The t-value (t stat) is not as large as in previous tests (Tables 6 and 7), indicating a smaller difference between the two groups, however it is still larger than the two-tail t-critical value. This means that a statistically significant difference between data for the low-Ti basalt and

bulk silicate Earth groups still exists. Please note that this version of the test includes all data from the previous test (Table 7) with the addition of the anomalous values for samples 12054.144,148 and 15535 included in the low-Ti data group. Sample 14053 was still omitted from this test due to the possibility of its petrogenesis being unrelated to the other mare basalts. The bulk silicate Earth group remained unchanged.

## REFERENCES

Benz, W., Cameron, A.G., and Melosh, H.J., 1989, The origin of the moon and the single-impact hypothesis III: Icarus, v. 81, p. 113–131.

Benz, W., Slattery, W.L., and Cameron, A.G.W., 1986, The origin of the moon and the single-impact hypothesis I: Icarus, v. 66, p. 515–535, doi:10.1016/0019-1035(86)90088-6.

Benz, W., Slattery, W.L., and Cameron, A.G.W., 1987, The origin of the moon and the single-impact hypothesis. II: Icarus, v. 71, p. 30–45, doi:10.1016/0019-1035(87)90160-6.

Bigeleisen, J., 1952, The effects of isotopic substitution on the rates of chemical reactions: The Journal of Physical Chemistry, v. 56, p. 823–828.

Bybee, G.M., 2014, High-pressure megacrysts and lower crustal contamination: Probing a mantle source for proterozoic massif-type anorthosites [PhD]: University of the Witwatersrand, 162 p., http://hdl.handle.net10539/14033 (accessed November 2018).

Cameron, A.G.W., 1997, The Origin of the Moon and the Single Impact Hypothesis V: Icarus, v. 126, p. 126–137, doi:10.1006/icar.1996.5642.

Cameron, A.G.W., and Benz, W., 1991, The origin of the moon and the single impact hypothesis IV: Icarus, v. 92, p. 204–216, doi:10.1016/0019-1035(91)90046-V.

Cameron, A.G.W., and Ward, W.R., 1976, The Origin of the Moon: Abstracts of the Lunar and Planetary Science Conference, v. 7, p. 120.

Cano, E.J., Sharp, Z.D., and Shearer, C.K., 2017, Mineral-specific variability of triple-oxygen isotope fractionation in lunar and terrestrial samples:

Canup, R.M., 2004, Dynamics of Lunar Formation: Annual Review of Astronomy and Astrophysics, v. 42, p. 441–475, doi:10.1146/annurev.astro.41.082201.113457.

Canup, R.M., 2012, Forming a Moon with an Earth-like Composition via a Giant Impact: Science, v. 338, p. 1052–1055, doi:10.1126/science.1226073.

Canup, R.M., and Asphaug, E., 2001, Origin of the Moon in a giant impact near the end of the Earth's formation: Nature, v. 412, p. 708–712, doi:10.1038/35089010.

Canup, R.M., Visscher, C., Salmon, J., and Jr, B.F., 2015, Lunar volatile depletion due to incomplete accretion within an impact-generated disk: Nature Geoscience, v. 8, p. 918–921, doi:10.1038/ngeo2574.

Chakraborty, S., Yanchulova, P., and Thiemens, M.H., 2013, Mass-Independent Oxygen Isotopic Partitioning During Gas-Phase SiO2 Formation: Science, v. 342, p. 463–466, doi:10.1126/science.1242237.

Chatzaras, V., Kruckenberg, S.C., Cohen, S.M., Medaris, L.G., Withers, A.C., and Bagley, B., 2016, Axial-type olivine crystallographic preferred orientations: The effect of strain geometry on mantle texture: Journal of Geophysical Research: Solid Earth, v. 121, p. 4895–4922, doi:10.1002/2015JB012628.

Craig, H., 1957, Isotopic standards for carbon and oxygen and correction factors for mass-spectrometric analysis of carbon dioxide: Geochimica et Cosmochimica Acta, v. 12, p. 133–149, doi:10.1016/0016-7037(57)90024-8.

Crumpler, L.S., 1980, An Alkali-Basalt through Trachyte Suite, Mesa Chivato Mount Taylor volcanic Field, New Mexico: GSA Bulletin, v. 91, p. 1293–1331, doi:10.1130/GSAB-P2-91-1293.

Ćuk, M., and Stewart, S.T., 2012, Making the Moon from a Fast-Spinning Earth: A Giant Impact Followed by Resonant Despinning: Science, v. 338, p. 1047–1052, doi:10.1126/science.1225542.

Dauphas, N. et al., 2014, Magma redox and structural controls on iron isotope variations in Earth's mantle and crust: Earth and Planetary Science Letters, v. 398, p. 127–140, doi:10.1016/j.epsl.2014.04.033.

Elkins-Tanton, L.T., Burgess, S., and Yin, Q.-Z., 2011, The lunar magma ocean: Reconciling the solidification process with lunar petrology and geochronology: Earth and Planetary Science Letters, v. 304, p. 326–336, doi:10.1016/j.epsl.2011.02.004.

Ernst, W.G., 1978, Petrochemical Study of Lherzolitic Rocks from the Western Alps: Journal of Petrology, v. 19, p. 341–392, doi:10.1093/petrology/19.3.341.

Frey, F.A., and Prinz, M., 1978, Ultramafic inclusions from San Carlos, Arizona: Petrologic and geochemical data bearing on their petrogenesis: Earth and Planetary Science Letters, v. 38, p. 129–176, doi:10.1016/0012-821X(78)90130-9.

Greenwood, R.C., Barrat, J.-A., Miller, M.F., Anand, M., Dauphas, N., Franchi, I.A., Sillard, P., and Starkey, N.A., 2018, Oxygen isotopic evidence for accretion of Earth's water before a high-energy Moon-forming giant impact: Science Advances, v. 4, p. eaao5928, doi:10.1126/sciadv.aao5928.

Gunn, B.M., 1966, Modal and element variation in Antarctic tholeiites: Geochimica et Cosmochimica Acta, v. 30, p. 881–920, doi:10.1016/0016-7037(66)90026-3.

Hallis, L.J., Anand, M., Greenwood, R.C., Miller, M.F., Franchi, I.A., and Russell, S.S., 2010, The oxygen isotope composition, petrology and geochemistry of mare

basalts: Evidence for large-scale compositional variation in the lunar mantle: Geochimica et Cosmochimica Acta, v. 74, p. 6885–6899, doi:10.1016/j.gca.2010.09.023.

Hartmann, W.K., and Davis, D.R., 1975, Satellite-sized planetesimals and lunar origin: Icarus, v. 24, p. 504–515, doi:10.1016/0019-1035(75)90070-6.

Hauri, E.H., Saal, A.E., Rutherford, M.J., and Van Orman, J.A., 2015, Water in the Moon's interior: Truth and consequences: Earth and Planetary Science Letters, v. 409, p. 252–264, doi:10.1016/j.epsl.2014.10.053.

Herwartz, D., Pack, A., Friedrichs, B., and Bischoff, A., 2014, Identification of the giant impactor Theia in lunar rocks: Science, v. 344, p. 1146–1150, doi:10.1126/science.1251117.

Hess, P.C., and Parmentier, E.M., 1995, A model for the thermal and chemical evolution of the Moon's interior: implications for the onset of mare volcanism: Earth and Planetary Science Letters, v. 134, p. 501–514, doi:10.1016/0012-821X(95)00138-3.

Hunt, C.B., 1938, Igneous geology and structure of the Mount Taylor volcanic field, New Mexico: Professional Paper USGS Numbered Series 189-B, http://pubs.er.usgs.gov/publication/pp189B (accessed November 2018).

Irving, A.J., 1975, Chemical, mineralogical and textural systematics of non-mare melt rocks: Implications for lunar impact and volcanic processes:, https://ntrs.nasa.gov/search.jsp?R=19750021901 (accessed October 2018).

Kamenetsky, V.S., Everard, J.L., Crawford, A.J., Varne, R., Eggins, S.M., and Lanyon, R., 2000, Enriched End-member of Primitive MORB Melts: Petrology and Geochemistry of Glasses from Macquarie Island (SW Pacific): Journal of Petrology, v. 41, p. 411–430, doi:10.1093/petrology/41.3.411.

Katayama, I., Suyama, Y., Ando, J., and Komiya, T., 2009, Mineral chemistry and P–T condition of granular and sheared peridotite xenoliths from Kimberley, South Africa: Origin of the textural variation in the cratonic mantle: Lithos, v. 109, p. 333–340, doi:10.1016/j.lithos.2008.05.004.

Kesson, S.E., and Ringwood, A.E., 1976, Mare basalt petrogenesis in a dynamic moon: Earth and Planetary Science Letters, v. 30, p. 155–163, doi:10.1016/0012-821X(76)90241-7.

Kimura, Y., Nuth, J.A., Chakraborty, S., and Thiemens, M.H., 2007, Non-mass-dependent oxygen isotopic fractionation in smokes produced in an electrical discharge: Meteoritics & Planetary Science, v. 42, p. 1429–1439, doi:10.1111/j.1945-5100.2007.tb00583.x.

Kohl, I.E., Warren, P.H., Schauble, E.A., and Young, E.D., 2017, Limitations on Δ'17O as a tracer of provenance revealed by mineral-specific values from lunar and terrestrial anorthosites, *in* Lunar Petrology and Geochemistry, The Woodlands, TX, v. 48, http://www.lpi.usra.edu/meetings/lpsc2017/pdf/sess502.pdf.

Kusakabe, M., Maruyama, S., Nakamura, T., and Yada, T., 2004, $CO_2$ Laser-$BrF_5$ Fluorination Technique for Analysis of Oxygen Three Isotopes of Rocks and Minerals: Journal of the Mass Spectrometry Society of Japan, v. 52, p. 205–212, doi:10.5702/massspec.52.205.

Lock, S.J., Stewart, S.T., Petaev, M.I., Leinhardt, Z., Mace, M.T., Jacobsen, S.B., and Cuk, M., 2018, The Origin of the Moon Within a Terrestrial Synestia: Journal of Geophysical Research: Planets, v. 123, p. 910–951, doi:10.1002/2017JE005333.

Luz, B., and Barkan, E., 2005, The isotopic ratios 17O/16O and 18O/16O in molecular oxygen and their significance in biogeochemistry: Geochimica et Cosmochimica Acta, v. 69, p. 1099–1110, doi:10.1016/j.gca.2004.09.001.

Mastrobuono-Battisti, A., Perets, H.B., and Raymond, S.N., 2015, A primordial origin for the compositional similarity between the Earth and the Moon: Nature, v. 520, p. 212–215, doi:10.1038/nature14333.

Melosh, H.J., 2014, New approaches to the Moon's isotopic crisis: Phil. Trans. R. Soc. A, v. 372, p. 20130168, doi:10.1098/rsta.2013.0168.

Melosh, H.J., and Kipp, M.E., 1989, Giant Impact Theory of the Moon's Origin: First 3-D Hydrocode Results, *in* v. 20, http://adsabs.harvard.edu/abs/1989LPI....20..685M (accessed June 2018).

Meyer, C., 2012, Lunar Sample Compendium: NASA Technical Report, https://curator.jsc.nasa.gov/lunar/compendium.cfm (accessed March 2017).

Miller, M.F., 2002, Isotopic fractionation and the quantification of 17O anomalies in the oxygen three-isotope system: an appraisal and geochemical significance: Geochimica et Cosmochimica Acta, v. 66, p. 1881–1889, doi:10.1016/S0016-7037(02)00832-3.

Miller, R., 1953, The webster-addie ultramafic ring, Jackson County, North Carolina, and secondary alteration of its chromite: American Mineralogist, v. 38, p. 1134–1147.

Norton, D., and Taylor, H.P., 1979, Quantitative Simulation of the Hydrothermal Systems of Crystallizing Magmas on the Basis of Transport Theory and Oxygen Isotope Data: An analysis of the Skaergaard Intrusion: Journal of Petrology, v. 20, p. 421–486, doi:10.1093/petrology/20.3.421.

Pack, A., and Herwartz, D., 2014, The triple oxygen isotope composition of the Earth mantle and understanding variations in terrestrial rocks and minerals: Earth and Planetary Science Letters, v. 390, p. 138–145, doi:10.1016/j.epsl.2014.01.017.

Pahlevan, K., and Stevenson, D.J., 2007, Equilibration in the aftermath of the lunar-forming giant impact: Earth and Planetary Science Letters, v. 262, p. 438–449, doi:10.1016/j.epsl.2007.07.055.

Phinney, W.C., 1969, RI-09 The Duluth Complex in the Gabbro Lake Quadrangle, Minnesota: Minnesota Geological Survey Report, http://conservancy.umn.edu/handle/11299/60307 (accessed November 2018).

Reid, A.M., and Jakes, P., 1974, Luna 16 Revisited: The case for Aluminous Mare Basalts: Abstracts of the Lunar and Planetary Science Conference, v. 5, http://adsabs.harvard.edu/abs/1974LPI.....5..627R (accessed October 2018).

Reufer, A., Meier, M.M.M., Benz, W., and Wieler, R., 2012, A hit-and-run giant impact scenario: Icarus, v. 221, p. 296–299, doi:10.1016/j.icarus.2012.07.021.

Ringwood, A.E., and Kesson, S.E., 1976, A dynamic model for mare basalt petrogenesis: Lunar and Planetary Science Conference Proceedings, v. 7, p. 1697–1722.

Saal, A.E., Hauri, E.H., Cascio, M.L., Van Orman, J.A., Rutherford, M.C., and Cooper, R.F., 2008, Volatile content of lunar volcanic glasses and the presence of water in the Moon's interior: Nature, v. 454, p. 192–195, doi:10.1038/nature07047.

Schonfeld, E., and Meyer, C., Jr., 1972, The abundances of components of the lunar soils by a least-squares mixing model and the formation age of KREEP: Proceedings of the Lunar Science Conference, v. 3, p. 1397.

Sharp, Z.D., 1990, A laser-based microanalytical method for the in situ determination of oxygen isotope ratios of silicates and oxides: Geochimica et Cosmochimica Acta, v. 54, p. 1353–1357, doi:10.1016/0016-7037(90)90160-M.

Sharp, Z.D., Barnes, J.D., Brearley, A.J., Chaussidon, M., Fischer, T.P., and Kamenetsky, V.S., 2007, Chlorine isotope homogeneity of the mantle, crust and carbonaceous chondrites: Nature, v. 446, p. 1062–1065, doi:10.1038/nature05748.

Sharp, Z.D., Gibbons, J.A., Maltsev, O., Atudorei, V., Pack, A., Sengupta, S., Shock, E.L., and Knauth, L.P., 2016, A calibration of the triple oxygen isotope fractionation in the SiO2–H2O system and applications to natural samples: Geochimica et Cosmochimica Acta, v. 186, p. 105–119, doi:10.1016/j.gca.2016.04.047.

Sharp, Z.D., Mercer, J.A., Jones, R.H., Brearley, A.J., Selverstone, J., Bekker, A., and Stachel, T., 2013, The chlorine isotope composition of chondrites and Earth: Geochimica et Cosmochimica Acta, v. 107, p. 189–204, doi:10.1016/j.gca.2013.01.003.

Sharp, Z.D., Wostbrock, J.A.G., and Pack, A., 2018, Mass-dependent triple oxygen isotope variations in terrestrial materials: Geochemical Perspectives Letters, v. 7, p. 27–31, doi:10.7185/geochemlet.1815.

Shearer, C.K. et al., 2006, Thermal and Magmatic Evolution of the Moon: Reviews in Mineralogy and Geochemistry, v. 60, p. 365–518, doi:10.2138/rmg.2006.60.4.

Shearer, C.K., and Papike, J.J., 1993, Basaltic magmatism on the Moon: A perspective from volcanic picritic glass beads: Geochimica et Cosmochimica Acta, v. 57, p. 4785–4812, doi:10.1016/0016-7037(93)90200-G.

Shearer, C.K., Papike, J.J., and Layne, G.D., 1996, Deciphering basaltic magmatism on the Moon from the compositional variations in the Apollo 15 very low-Ti picritic magmas: Geochimica et Cosmochimica Acta, v. 60, p. 509–528, doi:10.1016/0016-7037(95)00406-8.

Spera, F.J., 1992, Lunar magma transport phenomena: Geochimica et Cosmochimica Acta, v. 56, p. 2253–2265, doi:10.1016/0016-7037(92)90187-N.

Spicuzza, M.J., Day, J.M.D., Taylor, L.A., and Valley, J.W., 2007, Oxygen isotope constraints on the origin and differentiation of the Moon: Earth and Planetary Science Letters, v. 253, p. 254–265, doi:10.1016/j.epsl.2006.10.030.

Stevenson, D.J., and Halliday, A.N., 2014, The origin of the Moon: Phil. Trans. R. Soc. A, v. 372, p. 20140289, doi:10.1098/rsta.2014.0289.

Taylor, R.B., 1964, Bulletin No. 44. Geology of the Duluth Gabbro Complex near Duluth, Minnesota: Minnesota Geological Survey Map, http://conservancy.umn.edu/handle/11299/57070 (accessed November 2018).

Wang, K., and Jacobsen, S.B., 2016, Potassium isotopic evidence for a high-energy giant impact origin of the Moon: Nature, v. 538, p. 487–490, doi:10.1038/nature19341.

Warren, P.H., 1993, A concise compilation of petrologic information on possibly pristine nonmare Moon Rocks: American Mineralogist, v. 78, p. 360–376.

Wiechert, U., Halliday, A.N., Lee, D.-C., Snyder, G.A., Taylor, L.A., and Rumble, D., 2001, Oxygen Isotopes and the Moon-Forming Giant Impact: Science, v. 294, p. 345–348, doi:10.1126/science.1063037.

Wilhelm, S., and Wörner, G., 1996, Crystal size distribution in Jurassic Ferrar flows and sills (Victoria Land, Antarctica): evidence for processes of cooling, nucleation, and crystallisation: Contributions to Mineralogy and Petrology, v. 125, p. 1–15, doi:10.1007/s004100050202.

Young, E.D., Galy, A., and Nagahara, H., 2002, Kinetic and equilibrium mass-dependent isotope fractionation laws in nature and their geochemical and cosmochemical significance: Geochimica et Cosmochimica Acta, v. 66, p. 1095–1104, doi:10.1016/S0016-7037(01)00832-8.

Young, E.D., Kohl, I.E., Warren, P.H., Rubie, D.C., Jacobson, S.A., and Morbidelli, A., 2016, Oxygen isotopic evidence for vigorous mixing during the Moon-forming giant impact: Science, v. 351, p. 493–496, doi:10.1126/science.aad0525.

Zhong, S., Parmentier, E.M., and Zuber, M.T., 2000, A dynamic origin for the global asymmetry of lunar mare basalts: Earth and Planetary Science Letters, v. 177, p. 131–140, doi:10.1016/S0012-821X(00)00041-8.